3D mixed micromechanics-FEM modeling of piezoresistive carbon nanotube smart concrete

Enrique García-Macías[a,*], Rafael Castro-Triguero[c], Andrés Sáez[a], Filippo Ubertini[b]

[a]*Department of Continuum Mechanics and Structural Analysis, School of Engineering, Universidad de Sevilla , Camino de los Descubrimientos s/n, E-41092-Seville, Spain*
[b]*Department of Civil and Environmental Engineering, University of Perugia, Via G Duranti 93, Perugia 06125, Italy*
[c]*Department of Mechanics, University of Cordoba, Campus de Rabanales, Cordoba, CP 14071, Spain*

Highlights

- The 3D piezoresistivity matrix of CNT-reinforced smart concrete is obtained
- Strain sensitivity is studied by a mixed micromechanics-FEM approach
- Arbitrary 3D strain conditions are incorporated in the micromechanics model
- CNT-reinforced smart concrete three-dimensional structural elements are studied

Abstract

Within the novel approach for structural health monitoring of civil engineering structures based on smart self-sensing structural materials, Carbon NanoTube (CNT)-reinforced cement-based composites, often termed "smart concretes", have drawn rising interest. These composites exhibit self-sensing capabilities resulting in measurable variations of their electrical properties under applied mechanical deformations. This, along with the similarity between these composites and conventional structural concrete, makes it possible to devise cost-efficient distributed monitoring systems for large-scale Reinforced Concrete (RC) structures. While several papers in the literature have focused on pilot applications of smart concrete strain sensors embedded into large RC components, the response of these sensors is not yet fully understood at the fundamental physical level and, as a consequence, their output is not properly interpreted. In order to shed some light on this issue, previous work by the authors focused on laterally unconstrained uni-axial loading conditions. This work extends the previous studies by presenting a mixed micromechanics and finite element approach for the analysis of CNT-reinforced composites subjected to arbitrary strain states. The two mechanisms that contribute to the electrical conductivity of CNT-reinforced composites, namely electron hopping and conductive networking, are contemplated within a percolation framework in the micromechanics model. On the basis of the micromechanics model, the 3D piezoresistivity matrix is determined, for the first time in the literature, by means of virtual dilation and distortion tests. Afterwards, the electro-mechanical modeling of three-dimensional composite elements is conducted by a multi-physics finite element code. The potential of the presented approach is illustrated by extensive parametric analyses, as well as a comparison against experimental data, including application of the mixed micromechanics-finite-element multi-physics formulation for electro-mechanical modeling of three-dimensional elements.

Keywords: Carbon nanotube, Cement-based composites, Micromechanics, Piezoresistivity, Smart concrete, Structual Health Monitoring

1. Introduction

The recent development of novel multifunctional and smart structural materials, such as smart concretes and smart bricks, has led to a paradigm shift in the realm of structural health monitoring (SHM) of civil engineering structures towards self-sensing and self-inspecting buildings. In this new context, structural elements not only fulfill a structural function, but also behave as sensors apt for condition-based maintenance [1]. Carbon NanoTube (CNT) cement-based composites, often termed "smart concretes", have been shown particularly promising in the field of civil engineering with a broad spectrum of potential applications in the form of high-strength cement-based

*Corresponding author.
Email address: egarcia28@us.es (Enrique García-Macías)

composites [2, 3], embedded strain sensors for static [4] and dynamic [5] monitoring of RC structures, as well as in the form of smart portions of RC structures with direct crack detection capabilities [6]. These composites exhibit strain-sensing capabilities resulting in measurable variations of their electrical properties under applied mechanical deformations, that is a piezoresistive behavior [7, 8]. This unique property, along with the similarity between these composites and conventional concrete, suggests the possibility of developing distributed strain-sensing systems with considerable improvements in the cost-efficiency of the management of large-scale concrete structures [9–12]. Nonetheless, most theoretical works in the literature restrict their analyses to uni-axial loadings, whilst approaches capable of estimating the response of these composites under general three-dimensional strain states are sorely lacking.

Numerous experimental and theoretical studies agree to point out that the electrical conductivity of CNT-reinforced cement-based composites is governed by a percolation process [13–18]. On this basis, the overall electrical conductivity of these composites experiences a rapid increase when the filler concentration reaches a critical concentration, the so-termed percolation threshold. Below percolation, fillers are very distant and the transfer of electrons is only possible by an electron hopping mechanism, that is, a quantum tunneling effect. For increasing concentrations, only small increases are observed until fillers can touch each other resulting in a continuous electrically microscale conductive path, that is, the conductive networking mechanism. The percolation threshold thus corresponds to the onset of the formation of conductive paths. Hence, the strain-sensing capabilities of these composites are ascribed to strain-induced tampering of the electron hopping and the conductive networking mechanisms [19, 20]. In particular, three major changes are expected when CNT-reinforced composites are subjected to external mechanical strains [19, 21, 22]: (i) strain-induced changes in the volume fraction, (ii) changes in the conductive networks due to filler reorientation, and (iii) changes in the inter-particle properties.

In light of the outstanding potential of these composites as smart materials, most studies to date have been devoted to the experimental characterization and the development of new applications as strain sensors [4, 23–27]. Nevertheless, the number of theoretical studies that allow for tailoring the properties of these composites and for properly interpreting their outputs is much smaller. In this line, it is important to note the works of Deng and Zheng [28] and Takeda *et al.* [29] who incorporated the percolative-type behavior of CNT/polymer composites into a simplified micromechanics model of the overall electrical conductivity. Another noticeable contribution was made by Feng and Jiang [30] who proposed a Mori-Tanaka micromechanics model for the study of the individual influence of electron hopping and conductive networking mechanisms on the electrical conductivity of CNT/polymer composites. In that work, the electron hopping mechanism was simulated by means of conductive coatings surrounding the tubes, while the conductive networks were accounted for by changes in the fillers aspect ratios. Concerning the strain sensitivity of CNT-reinforced composites, the number of works is considerably lower. It is worth noting the contribution of Alamusi and Hu [31] who utilized a three-dimensional resistor network previously proposed by Hu *et al.* [32], incorporating Simmon's contact resistance among CNTs [33] along with a fiber re-orientation model [34]. Tallman and Wang [21] extended the theoretical formulation developed by Takeda *et al.* [29] for the piezoresistivity modeling of CNT composites subjected to arbitrary dilations. In that work, the strain-induced variation of the percolation threshold was simulated by a simplified excluded volume approach [35]. Their results demonstrated that the strain sensitivity of CNT-reinforced composites is defined by a first linear stage, followed by a non-linear one. Moreover, those authors showed that the non-linear contribution is higher for filler concentrations near the percolation threshold. Another important contribution is due to Feng and Jiang [19] who focused on the modeling of uni-axial strain self-sensing properties of CNT/polymer composites. In that work, the authors presented closed-form expressions of the Orientation Distribution Functions (ODFs) of random fiber configurations under the action of laterally unconstrained axial stretching. Afterwards, the authors [22] presented a mixed Mori-Tanaka micromechanics approach for the modeling of the laterally unconstrained uni-axial strain sensitivity of CNT-reinforced cement-based composites. In that work, the strain-induced variation of the percolation threshold was related to the filler-reorientation by means of ODFs. The results demonstrated that the strain-sensitivity is maximum at the percolation threshold, and very good agreement with experimental data was found. The case of bi-axial stretching was also studied by Feng and Jiang [36] who presented closed-form expressions of the ODFs for such loading configurations. It should be also remarked the recent work by Wang *et al.* [37] who developed a two-dimensional representative volume element to simulate the electromechanical response of silicone elastomer doped with Carbon Black (CB). In that work, comparison analyses against experimental data for laterally constrained uni-axial stretching demonstrated the importance of large deformation effects on the non-linear electrical response of the composites. Notwithstanding these developments, there is no generalized micromechanical scheme allowing for the modeling of the electro-mechanical response of CNT-reinforced cement-matrix composites under arbitrary 3D strain states. This present work is intended to address this gap.

In view of the above-mentioned lacuna in the literature, this paper is aimed at devising a micromechanics approach in combination with a three-dimensional finite element formulation for the analysis of the response of CNT-reinforced smart concretes subjected to arbitrary strain states. This study is a 3D generalization of the

micromechanics models of the overall conductivity and uniaxial piezoresistivity, recently proposed by the authors in [38] and [22]. The two mechanisms that contribute to the conductivity of CNT-reinforced composites, namely electron hopping and conductive networking, are contemplated in the mixed micromechanics framework. The origin of the piezoresistive response of these composites is attributed to (i) strain-induced changes in the volume fraction, (ii) changes in the conductive networks due to the filler reorientation and, therefore, the percolation threshold, and finally, (iii) changes in the tunneling resistance through variation of the inter-particle distance and the height of the potential barrier. New closed-form expressions for ODFs of random arrangements of fillers under arbitrary dilations and distortions are presented. Moreover, waviness and agglomeration of fillers in bundles can be readily incorporated in a similar way to previous work by the authors. Assuming that the piezoresistivity matrix possesses cubic crystal symmetry, the piezoresistivity coefficients can be determined by two virtual loading cases, namely laterally constrained compression/stretching, and shear strain. In this way, an approximate simplified model for smart concrete strain sensors easy to handle in practical applications is also proposed. Afterwards, the electro-mechanical constitutive relation is included in a multi-physics Finite Element Model (FEM) formulation to achieve a general computational tool able to map the strain-induced alterations of the electrical resistivity of composites when sustaining a general strain field in a variety of full-scale applications. The potential of the proposed approach is illustrated by detailed parametric analyses and comparison against experimental data, as well as the application for electro-mechanical modeling of three-dimensional elements.

The paper is organized as follows. Section 2 concisely overviews previous work by the authors on the modeling of the overall electrical conductivity, as well as the uni-axial piezoresistivity of CNT-reinforced composites. Section 3 presents an extension of those previous approaches for the modeling of arbitrary dilations and distortions. Section 4 describes the definition of the complete piezoresistivity matrix and its incorporation in a three-dimensional electro-mechanical framework. Section 5 presents the numerical results and, eventually, Section 6 concludes the paper.

2. Review of micromechanics modeling of laterally unconstrained uniaxial piezoresistivity of CNT-reinforced cement-matrix composites

This section overviews the micromechanics approaches of the overall conductivity and laterally unconstrained uni-axial piezoresistivity of cement-matrix composites with CNTs, recently proposed by the authors in references [38] and [22]. Let us first define a Representative Volume Element (RVE) consisting of a cementitious matrix doped with a sufficient number of fillers in such a way that the overall properties of the composite are statistically represented [39]. The two mechanisms underlying the electronic transport properties of these composites, namely electron hopping and conductive networking, are incorporated in a mixed micromechanics framework as schematically depicted in Fig. 1. The quantum tunneling effect associated with the electron hopping mechanism is accounted for by means of conductive interfaces surrounding the nanotubes. With regard to the conductive networking mechanism, the formation of percolative paths is simulated by changes in the fillers aspect ratios. In this context, the appearance of external strains provokes changes in both mechanisms and, thus, changes in the overall conductivity. In particular, most literature works agree to list the foremost strain-induced changes as (i) volume expansion and consequent change in the filler volume fraction, (ii) filler reorientation and, therefore, changes in the percolation threshold and, finally, (iii) changes in the tunneling resistance through variation of the inter-particle properties.

2.1. Electrical conductivity of unstrained CNT-reinforced composites

Following a percolative-type behavior, when the CNT volume fraction f is below the percolation threshold f_c, CNTs are electrically independent and solely contribute to the overall conductivity of the composite by means of electron hopping mechanism. Once the CNT volume fraction reaches the percolation threshold, some fillers begin forming conductive networks and the overall electrical conductivity is controlled by both mechanisms simultaneously.

Electron hopping mechanism is characterized by a quantum tunneling effect through which electrons can migrate between proximate non-connected fillers. The cut-off distance for tunneling effects, that is, the maximum possible separation between two CNTs within the cementitious matrix that permits the tunneling penetration of electrons, is taken as $d_c = 0.5$ nm as reported by Wen and Chung [40]. When the volume fraction is below the percolation threshold ($f < f_c$), the average distance between CNTs without electrical contacts d_a is presumably larger than d_c, however, due to the difficulty in estimating its value, it is simplified as $d_a = d_c$. On the other hand, for volume fractions above the percolation threshold ($f \geq f_c$), the average separation distance d_a between adjacent CNTs has been reported to follow a power-law description [30]:

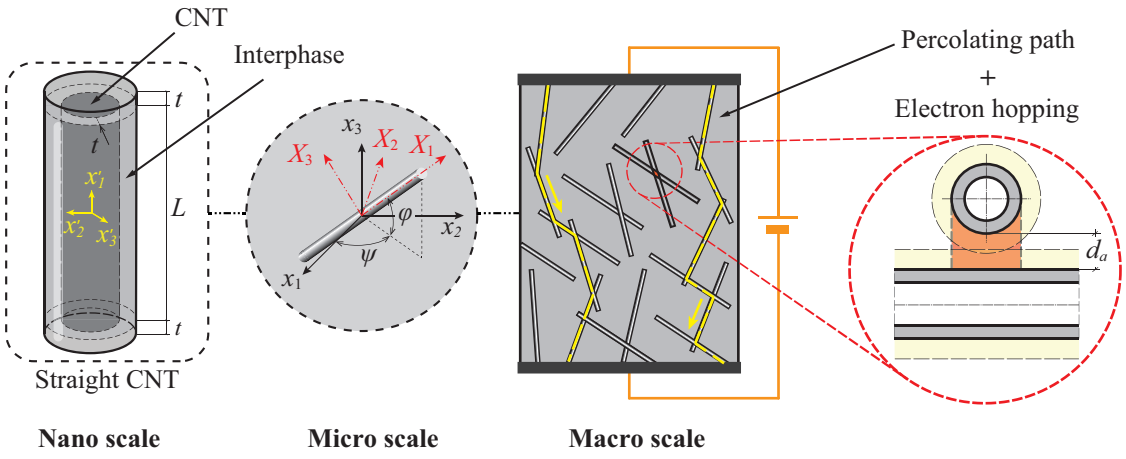

Figure 1: Schematic representation of a RVE including straight CNTs and the contribution of electron hopping and conductive network mechanisms to the overall electrical conductivity of CNT nanocomposites.

$$d_a = \begin{cases} d_c & 0 \le f < f_c \\ d_c \left(\dfrac{f_c}{f}\right)^{1/3} & f_c \le f \le 1 \end{cases} \tag{1}$$

In addition, the electrical contact resistance of the interface can be estimated by the generalized Simmons formula [41] as follows:

$$R_{int}(d_a) = \frac{d_a \hbar^2}{a e^2 \left(2m\lambda^{1/2}\right)} \exp\left(\frac{4\pi d_a}{\hbar} \left(2m\lambda\right)^{1/2}\right) \tag{2}$$

where m and e are the mass and the electric charge of an electron, respectively, λ is the height of the tunneling potential barrier (taken as 0.36 eV for cement-based materials [40]), a is the contact area of the CNTs and $\hbar$ stands for the reduced Planck's constant. Hence, electron hopping mechanism can be simulated by means of conducting inter-phases around the CNTs with thickness t and electrical conductivity σ_{int} [30, 42]:

$$t = \frac{1}{2} d_a, \quad \sigma_{int} = \frac{d_a}{a R_{int}(d_a)} \tag{3}$$

The equivalent composite cylinder assemblage thus consists of a CNT (length L and diameter $D = 2r_c$) and a surrounding inter-phase of thickness t (see Fig. 1). The conductivity tensor of the equivalent solid cylinder, $\boldsymbol{\sigma}_c$, is defined as transversely isotropic in the local coordinate system $\{X_1, X_2, X_3\}$ with effective longitudinal $\tilde{\sigma}^L$ and transverse $\tilde{\sigma}^T$ electrical conductivities. By applying Maxwell's equations and the law-of-mixture rule, $\tilde{\sigma}^L$ and $\tilde{\sigma}^T$ can be written as [30, 43]:

$$\tilde{\sigma}^L = \frac{(L+2t)\sigma_{int}\left[\sigma_c^L r_c^2 + \sigma_{int}\left(2r_c t + t^2\right)\right]}{2\sigma_c^L r_c^2 t + 2\sigma_{int}\left(2r_c t + t^2\right) t + \sigma_{int} L \left(r_c + t\right)^2}, \tag{4a}$$

$$\tilde{\sigma}^T = \frac{\sigma_{int}}{L+2t}\left[L \frac{2r_c^2 \sigma_c^T + \left(\sigma_c^T + \sigma_{int}\right)\left(t^2 + 2r_c t\right)}{2r_c^2 \sigma_{int} + \left(\sigma_c^T + \sigma_{int}\right)\left(t^2 + 2r_c t\right)} + 2t\right] \tag{4b}$$

and the volume fraction f_{eff} of the effective solid fillers, i.e. fillers and interphases, reads:

$$f_{eff} = \frac{\left(r_c + t\right)^2 \left(L + 2t\right)}{r_c^2 L} f \tag{5}$$

The overall properties of the RVE consisting of matrix and equivalent composite cylindrical inclusions can be estimated by mean-field homogenization techniques. In particular, the Mori-Tanaka method [44] has been shown accurate for moderate filler concentrations, as it is typically the case of CNT-reinforced cement-matrix composites. For its implementation, the orientation of every inclusion aligned in the local X_1 direction is specified by two Euler angles, φ and ψ. Hence, the Mori-Tanaka estimation of the overall electrical conductivity of the RVE reads [45]:

$$\boldsymbol{\sigma}_{eff} = \boldsymbol{\sigma}_m + f_{eff} \langle (\boldsymbol{\sigma}_c - \boldsymbol{\sigma}_m) \boldsymbol{A} \rangle \tag{6}$$

with $\boldsymbol{\sigma}_c$ and $\boldsymbol{\sigma}_m$ being the conductivity tensors of the effective fillers and the matrix, respectively. The angle brackets $\langle \cdot \rangle$ stand for averaging over all possible orientations in the Euler space. Considering a tensor $\boldsymbol{F}$ in the local coordinate system, its orientational average, $\langle \boldsymbol{F} \rangle$, is defined through:

$$\langle \boldsymbol{F} \rangle = \int_0^{2\pi} \int_0^{\pi/2} \boldsymbol{Q}^T \boldsymbol{F} \boldsymbol{Q} p(\psi, \varphi) \sin(\varphi) \mathrm{d}\varphi \mathrm{d}\psi \tag{7}$$

where $p(\varphi, \psi)$ is the ODF, and $\boldsymbol{Q}$ is the rotation matrix. The electric field concentration tensor, $\boldsymbol{A}$, can be expressed in the local coordinate system as [30]:

$$\boldsymbol{A} = \boldsymbol{A}^{dil} \left\{ \left(1 - f_{eff}\right) \boldsymbol{I} + f_{eff} \left\langle \boldsymbol{A}^{dil} \right\rangle \right\}^{-1} \tag{8}$$

with $\boldsymbol{A}^{dil}$ being the dilute electric field concentration tensor:

$$\boldsymbol{A}^{dil} = \left\{ \boldsymbol{I} + \boldsymbol{S} (\boldsymbol{\sigma}_m)^{-1} (\boldsymbol{\sigma}_c - \boldsymbol{\sigma}_m) \right\}^{-1} \tag{9}$$

where $\boldsymbol{I}$ is the second-order identity tensor and $\boldsymbol{S}$ the Eshelby's tensor. The Eshelby's tensor, well documented in [46], depends upon the inclusion geometry and the hosting matrix.

According to the percolation theory, for CNT volume fractions below the percolation threshold, $f < f_c$, electron hopping mechanism controls the overall conductivity of the composite and, therefore, the fraction of percolated CNTs, ξ, is null. Conversely, once percolation starts, $f \geq f_c$, a rising number of CNTs starts forming conductive networks. As reported by Deng and Zheng [28], ξ can be approximately estimated as:

$$\xi = \begin{cases} 0, & 0 \leq f < f_c \\ \dfrac{f^{1/3} - f_c^{1/3}}{1 - f_c^{1/3}}, & f_c \leq f \leq 1 \end{cases} \tag{10}$$

From the derivation above, it follows that the overall electrical conductivity of CNT-reinforced nanocomposites in Eq. (6) can be extended by including the simultaneous contribution of both mechanisms as:

$$\begin{aligned} \boldsymbol{\sigma}_{eff} =& \boldsymbol{\sigma}_m + (1 - \xi) \left\langle f_{eff} (\boldsymbol{\sigma}_{EH} - \boldsymbol{\sigma}_m) \boldsymbol{A}_{EH} \right\rangle + \\ &+ \xi \left\langle f_{eff} (\boldsymbol{\sigma}_{CN} - \boldsymbol{\sigma}_m) \boldsymbol{A}_{CN} \right\rangle \end{aligned} \tag{11}$$

where subscripts EH and CN refer to electron hopping and conductive networking mechanisms, respectively. In the case of CNTs forming conductive networks, several nanotubes are electrically connected in a continuous conductive path. This effect can be modeled by considering fillers with infinite aspect ratio [42]. As a result, the quantities associated with the electron hopping mechanism are defined with the real fillers aspect ratio ($a_2 = a_3 = r_c$, $a_1 = L$), while quantities corresponding to conductive networks are defined with an infinite aspect ratio ($a_2 = a_3 = r_c$, $a_1 \to \infty$).

Finally, it is important to note that this micromechanics approach offers a suitable framework for including waviness and agglomeration effects. Details on the formulation of these two phenomena have been omitted in this work due to space constraints. For more information on this aspect, readers are invited to read Sections 2.2 and 2.3 in reference [22].

2.2. Laterally unconstrained uni-axial piezoresistivity of CNT-reinforced composites

As mentioned above, the strain sensing capability of CNT-reinforced composites is ascribed to strain-induced alterations of the physical mechanisms that govern the overall conductivity, including (i) volume expansion and reorientation of CNTs, (ii) breakage/formation in the conductive networks, and (iii) changes in the tunneling resistance. These mechanisms are briefly recalled below.

2.2.1. Volume expansion and reorientation of CNTs

Let us consider a deformable cubic cell of side l_o containing an embedded filler after the application of a laterally unconstrained uniaxial strain ε as shown in Fig. 2. The change of the initial volume of the cell $V_o = l_o^3$ can be determined by the general expression $V = l_o^3 (1 + \varepsilon)^{1-2\nu}$, with ν being the Poisson's ratio of the composite. For small deformations, the volume of the strained cell can be reduced to $V = l_o^3 (1 + \varepsilon)(1 - \nu\varepsilon)^2$. Moreover, assuming that the deformation of the composite is sustained by the matrix, the volume of the nano-inclusions

remains constant and, therefore, the volume expansion also leads to changes in the CNT volume fraction, such that the modified volume fraction, f^*, is equal to [19]:

$$f^* = \frac{V_o f}{V} = \frac{f}{(1+\varepsilon)^{1-2\nu}} \tag{12}$$

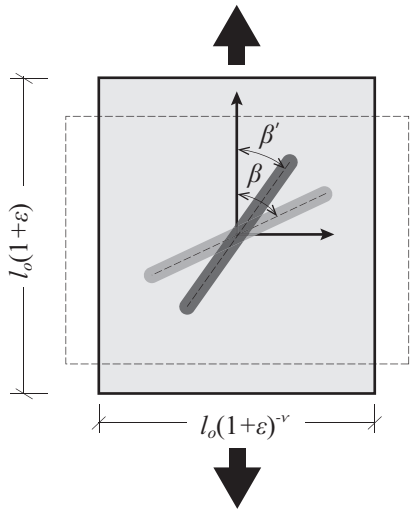

Figure 2: Schematic representation of the volume expansion and reorientation of a conductive filler within a deformable cell subjected to laterally unconstrained uni-axial strain ε.

Likewise, it can be noted in Fig. 2 that the strain ε also originates a re-orientation of the filler. This change of orientation is characterized by a change of the polar angle from β to β', with negligible variation of the azimuth angle ψ [19]. After the application of strain, the initially randomly oriented fillers ($p(\psi,\beta) = 1$) tend to align in the strain direction and vice versa. Under the assumption of a constant number of fillers throughout the composite, Feng and Jiang [19] obtained a closed-form expression of the ODF of random filler arrangements under laterally unconstrained uni-axial strains as follows:

$$p(\beta') = \frac{(1+\varepsilon)^{\frac{1+\nu}{2}}}{\left[(1+\varepsilon)^{-(1+\nu)}\cos^2(\beta') + (1+\varepsilon)^{(1+\nu)}\sin^2(\beta')\right]^{\frac{3}{2}}} \tag{13}$$

2.2.2. Change in the conductive networks

The reorientation of the fillers decreases the randomness of the CNT distribution and, consequently, also reduces the probability of forming conductive paths. In other words, the reorientation of the fillers leads to increments in the percolation threshold f_c. The variation of the percolation threshold can be associated to the ODF as shown in [47] and [22]. According to the Komori and Makishima approach [48], the mean distance between contacts, $\overline{b}$, is given by:

$$\overline{b} = \frac{\pi D}{8 I f} \tag{14}$$

where

$$I = \int_0^{\pi} \mathrm{d}\varphi \int_0^{\pi} J(\psi,\varphi) p(\psi,\varphi) \sin\varphi \mathrm{d}\psi \tag{15}$$

$$J(\varphi,\psi) = \int_0^{\pi} \mathrm{d}\varphi' \int_0^{\pi} \sin\tau\, p(\psi',\varphi') \sin\varphi' \mathrm{d}\psi' \tag{16}$$

$$\sin\tau = \left[1 - \{\cos\varphi\cos\varphi' + \cos(\psi-\psi')\sin\varphi\sin\varphi'\}^2\right]^{1/2} \tag{17}$$

Each filler must have at least two contact points to be part of a conductive path in the nanocomposite [49] or, alternatively, the mean distance between contacts must be at least half of the filler length. Kumar and Rawal [47] defined a coverage parameter, $\Gamma = b/L$, which stands for the number of contacts formed along a given filler length so that this quantity is $\Gamma \leq 0.5$ for percolated nanofillers. Furthermore, a mean coverage parameter, $\overline{\Gamma} = \overline{b}/L$, can

be defined as the probability of percolation of the composite. Finally, it has been reported in the literature that the distance between contacts follows an exponential distribution [50, 51], and similarly, the probability density function of the coverage parameter Γ can be defined as [47]:

$$P(\Gamma) = (1/\overline{\Gamma})\exp\left(-\Gamma/\overline{\Gamma}\right) \tag{18}$$

Zheng *et al.* [52] reported that the statistical percolation threshold is reached when 50% of the sample percolates, this is:

$$\int_0^{0.5} P(\Gamma)\mathrm{d}\Gamma = -\exp(0.5/\overline{\Gamma}) + 1 = 0.5 \tag{19}$$

where a value $\overline{\Gamma}$ of 0.72 is extracted. Finally, combining this result with Eq. (14), the percolation threshold can be computed using the Komori-Makishima model as:

$$f_c = \frac{\pi}{5.77sI} \tag{20}$$

with s being the aspect ratio of the nanofillers, i.e. L/D.

2.2.3. Change in the tunneling resistance

Finally, a third strain-induced alteration on the microstructure of the composite relates to the variation of the inter-particle properties. In particular, it is apparent that under the action of external strains, the separation of fillers changes and, consequently, the electron hopping mechanism so does. It has been reported in the literature that the change of the fillers resistance is assumed negligible because of the extremely small deformation in nanotubes resulting from their high elastic modulus. Conversely, larger deformations are experienced by the inter-nanotube matrix due to its relatively low modulus, what contributes to the electrical resistance change of the composite [53]. Hence, some research studies assume that, at relatively low strains ($< 10^{-4}$), the inter-particle distance and the height of the potential barrier change proportionally to the strain [54] as follows:

$$\begin{aligned} d_a &= d_{a,0}(1 + C_1\varepsilon), \\ \lambda &= \lambda_0(1 + C_2\varepsilon) \end{aligned} \tag{21}$$

where $d_{a,0}$ and λ_0 are the initial inter-particle distance and potential height of the unstrained system. Due to the lack of information in the literature about explicit expressions for these quantities, the proportionality constants C_1 and C_2 have to be obtained by fitting experimental data. For instance, in reference [22], values of C_1=5.0, C_2=1.5 were obtained for mortar doped with MWCNTs.

3. Extension of micromechanics modeling to 3D piezoresistivity of CNT-reinforced cement-matrix composites

In this section, the previously reviewed formulation is extended to account for general three-dimensional strain states. It is important to note that the previous formulation is only valid for laterally unconstrained uniaxial compression/tension tests and, therefore, it does not make it possible to map the strain-induced variations of the electrical conductivity of 3D structural elements when subjected to arbitrary strain fields. In order to fill this lacuna, this section presents a novel micromechanics approach to analyze both general dilation and distortion strain states. In this way, it is possible to construct three-dimensional piezoresistivity matrices, apt to be applied to steady-state piezoresistivity analyses in a FEM code as shown in the next section. In a similar way to the previous section, strain-induced alterations are divided into (i) volume expansion and reorientation of fillers, (ii) changes in the conductive networks, and (iii) changes in the tunneling resistance.

3.1. Volume expansion and reorientation of CNTs under 3D strain states

Two different strain states are considered, namely dilation and distortion. The main purpose of this section is to study the volume expansion and fillers reorientation under both strain conditions. New closed-form expressions of the ODFs are presented for affine deformation of cubic cells of random arrangements of fillers under three-dimensional dilation strains and shear.

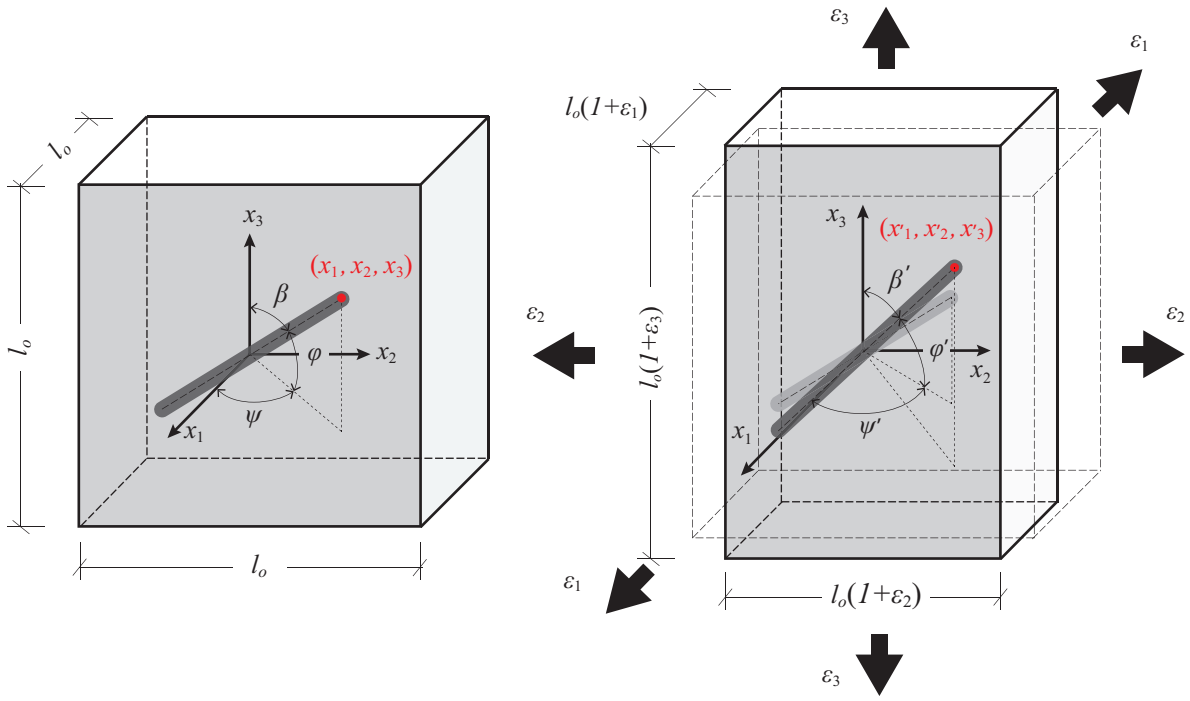

Figure 3: Schematic representation of the volume expansion and reorientation of a conductive filler within a deformable cell subjected to a triaxial strain state $(\varepsilon_1, \varepsilon_2, \varepsilon_3)$.

3.1.1. Dilation strain

Let us retake the deformable cubic cell of side l_o, loaded with an embedded filler before and after the application of a 3D strain state $(\varepsilon_1, \varepsilon_2, \varepsilon_3)$ as shown in Fig. 3. The volume of the cell changes from $V_o = l_o^3$ to $V = l_o^3 (1+\varepsilon_1)(1+\varepsilon_2)(1+\varepsilon_3) = l_o^3 \bar{\varepsilon}_1 \bar{\varepsilon}_2 \bar{\varepsilon}_3$. It is assumed that the filler remains inextensible because its stiffness is considerably higher than that of the matrix. In this way, the deformation of the composite is mainly sustained by the matrix and, therefore, the volume expansion induces changes in the CNT volume fraction as follows:

$$f^* = \frac{V_o f}{V} = \frac{f}{\bar{\varepsilon}_1 \bar{\varepsilon}_2 \bar{\varepsilon}_3} \tag{22}$$

Likewise, it can be noted from Fig. 3 that the strains also originate a re-alignment of the fiber. This change of orientation is characterized by a change of the Euler angles from (β, ψ) to (β', ψ'). Correspondingly, the relationships between the coordinates of the upper end of the filler in the cell before (x_1, x_2, x_3) and after (x_1', x_2', x_3') the application of the tri-axial strain are determined in terms of the Euler angles as:

$$\frac{x_1'}{x_1} = \frac{u' \sin\beta' \cos\psi'}{u \sin\beta \cos\psi} = \bar{\varepsilon}_1 \tag{23}$$

$$\frac{x_2'}{x_2} = \frac{u' \sin\beta' \sin\psi'}{u \sin\beta \sin\psi} = \bar{\varepsilon}_2 \tag{24}$$

$$\frac{x_3'}{x_3} = \frac{u' \cos\beta'}{u \cos\beta} = \bar{\varepsilon}_3 \tag{25}$$

where u and u' are the half lengths of the filler before and after the application of the dilation. Since the filler is considerably stiffer than the matrix, it is assumed as inextensible, that is $u' = u$. This change of the Euler angles of the fillers results in a change of the ODF from $p(\psi, \beta)$ to $p(\psi', \beta')$. After the application of strain, the initially randomly oriented fillers ($p(\psi, \beta) = 1$) tend to re-align and, therefore, the randomness of the nanofillers arrangement is reduced. In order to obtain the resulting ODF, the condition of a constant number of fillers before and after the application of the strain can be applied. In this regard, considering a total number of G fillers distributed in the RVE, the number of fillers, $\mathrm{d}N$, lying in the orientation range $(\beta, \beta + \mathrm{d}\beta) \times (\psi, \psi + \mathrm{d}\psi)$ can be computed as [19]:

$$\mathrm{d}N_{\substack{\beta,\beta+\mathrm{d}\beta \\ \psi,\psi+\mathrm{d}\psi}} = \frac{1}{\pi} G p(\psi, \beta) \sin\beta \mathrm{d}\beta \mathrm{d}\psi \tag{26}$$

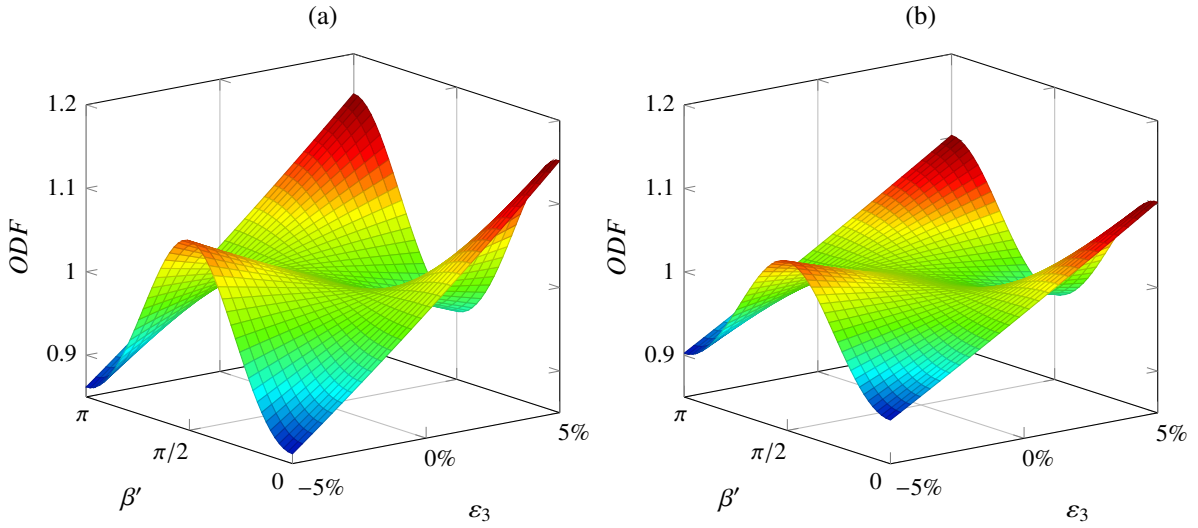

Figure 4: Variation of $p(\psi',\beta')$ (ODF) with strain ε_3 and polar angle β' for laterally unconstrained (a) and constrained (b) conditions ($\nu = 0.45$).

The total number of fillers must remain constant after the application of the strain within the range $(\beta',\beta' + \mathrm{d}\beta') \times (\psi',\psi' + \mathrm{d}\psi')$, what yields:

$$\mathrm{d}N_{\substack{\beta',\beta'+\mathrm{d}\beta' \\ \psi',\psi'+\mathrm{d}\psi'}} = \mathrm{d}N_{\substack{\beta,\beta+\mathrm{d}\beta \\ \psi,\psi+\mathrm{d}\psi}} \tag{27}$$

Substituting Eqs. (25-26) into Eq. (27), and considering that $p(\psi,\beta) = 1$ since CNTs are assumed randomly oriented in the undeformed configuration, the resulting ODF, $p(\psi',\beta')$, is determined after some manipulations as:

$$p(\psi',\beta') = \frac{\overline{\varepsilon}_1^2\overline{\varepsilon}_2^2\overline{\varepsilon}_3^2}{\left[\overline{\varepsilon}_2^2\overline{\varepsilon}_3^2\cos^2\beta' + \overline{\varepsilon}_1^2\left(\overline{\varepsilon}_2^2\cos^2\psi' + \overline{\varepsilon}_3^2\sin^2\psi'\right)\sin^2\beta'\right]^{3/2}} \tag{28}$$

In the absence of strains, i.e. $\varepsilon_1 = \varepsilon_2 = \varepsilon_3 = 0$ or equivalently $\overline{\varepsilon}_1 = \overline{\varepsilon}_2 = \overline{\varepsilon}_3 = 1$, the ODF in Eq. (28) reduces to unity as expected for a random orientation distribution. Figs. 4 (a) and (b) show the variation of the ODF with the uni-axial strain ε_3 and the polar angle β for laterally unconstrained ($1 + \varepsilon_1 = 1 + \varepsilon_2 = (1 + \varepsilon_3)^{-\nu}$) and constrained conditions ($\varepsilon_1 = \varepsilon_2 = 0$), respectively. The axial strain ε_3 is defined varying from -5% (compression) to +5% (tension). It is noted that such high strain values are not physical for concrete and cement-based materials, but are here considered for generality, as the derived ODFs can be used for different CNT-reinforced composites, as well as for illustrative purposes. In both cases, when strains are zero, the ODF remains constant and equal to 1 for every polar angle, corresponding to the random orientation distribution case as previously indicated. It is also observed that, for increasing stretching ($\varepsilon_3 > 0$), the ODF gives more weight to polar angles close to 0 and π, what indicates that more nanotubes tend to re-align in the direction of the strain. On the contrary, for increasing compression ($\varepsilon_3 < 0$), the ODF has higher values for polar angles around $\pi/2$ and, therefore, the nanotubes tend to re-align in the transverse direction of the strain. With regard to the lateral conditions, it is observed that the randomness of the orientation is less altered when the composite is laterally constrained.

Fig. 5 (a) shows the ODF under bi-axial stretching with $\varepsilon_3 = 5\%$ and $\varepsilon_2 = 0.25{\cdot}5\%$ and laterally unconstrained condition, that is, $\overline{\varepsilon}_1 = [(1 + \varepsilon_3)(1 + \varepsilon_2)]^{-\frac{\nu}{1-\nu}}$. Similarly, Fig. 5 (b) shows the ODF under bi-axial stretching with $\varepsilon_3 = \varepsilon_2 = 5\%$ and laterally unconstrained condition. From these figures, it can be seen that the strain tends to re-align the fillers along the stretching directions ($\psi = \pi/2$ and $\beta = 0, \pi$). Comparing the ODFs in Figs. 5 (a) and (b), it is concluded that increasing the stretching in the x_2 direction increases the re-alignment of fillers along that direction.

Finally, in order to further the comprehension of Eq. (28), the ODFs obtained for uni-axial stretching along the (a) x_1, (b) x_2 and (c) x_3 directions with laterally constrained conditions are depicted in Fig. 6. It is observed that, in all cases, stretching induces a re-alignment of the fillers in the strain direction.

3.1.2. Distortion strain

Let us now consider a deformable cubic cell containing an embedded filler before and after the application of a distortion ε_{32} as shown in Fig. 7. In this case, distortion does not originate any volume change although it does induce re-orientation of the filler. In order to study the deformed configuration, two auxiliary planes A and B are

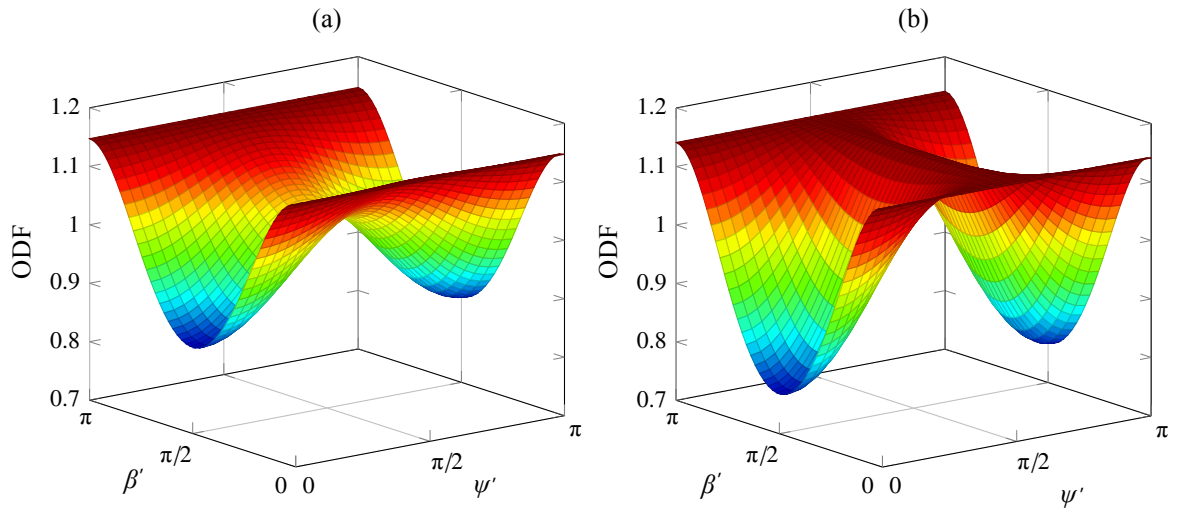

Figure 5: Variation of $p(\psi', \beta')$ (ODF) with polar β' and azimuthal angle ψ' under bi-axial stretching (a) $\varepsilon_3 = 5\%, \varepsilon_2 = 0.25 \cdot 5\%$ and (b) $\varepsilon_3 = 5\%, \varepsilon_2 = 5\%$ in laterally unconstrained conditions ($\nu = 0.45$).

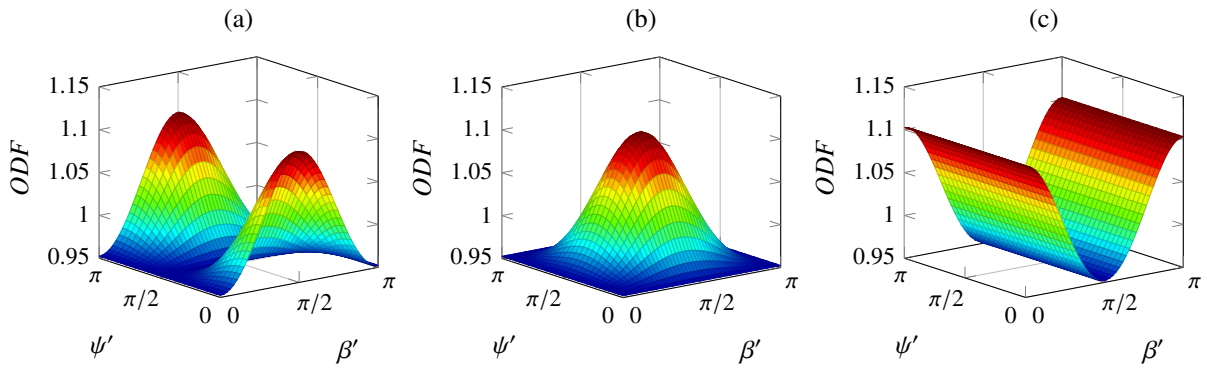

Figure 6: Variation of $p(\psi', \beta')$ (ODF) with polar β' and azimuthal angle ψ' with uni-axial stretching along the (a) x_1, (b) x_2 and (c) x_3 directions under laterally constrained conditions ($\varepsilon_i = 5\%, \overline{\varepsilon}_j = 1 \; j \neq i, \nu = 0.45$).

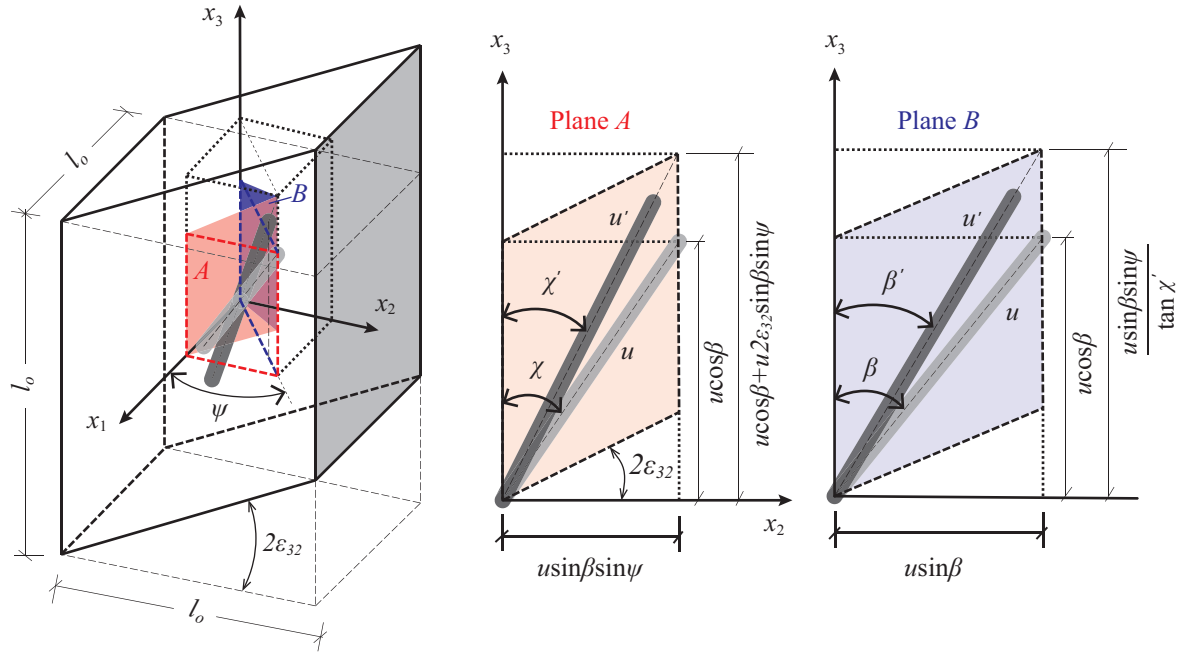

Figure 7: Schematic representation of reorientation of a conductive filler within a deformable cell subjected to a distortion ε_{32}.

defined as indicated in the figure. Plane A is parallel to the $x_2 - x_3$ plane and contains the upper end of the filler. On the other hand, plane B is defined by the x_3-axis and the upper end of the filler. An auxiliary angle χ is defined as the angle between the x_3-axis and the orthogonal projection of the filler onto plane A. It is observed that once the distortion is applied, both planes transform into rhombuses. It is hypothesized that the filler re-aligns in the diagonal direction of both rhombuses. Hence, this assumption completely determines the orientation of the filler after the application of strain, irrespective of the deformed filler length u'. In a similar way to the previous case, it is assumed that the strain is mainly held by the matrix and the filler is assumed inextensible, i.e. $u' = u$. In the particular case of ε_{32}, it is also observed that the polar angle changes from β to β', while the azimuthal angle remains unaltered. Using trigonometric relations in Fig. 7, the following relations can be extracted:

$$\tan\chi' = \frac{\sin\beta\sin\psi}{\cos\beta + 2\varepsilon_{32}\sin\beta\sin\psi} \tag{29}$$

$$\tan\beta' = \frac{\tan\chi'}{\sin\psi} \tag{30}$$

and substitution of Eq. (29) into Eq. (30) leads to:

$$\tan\beta = \frac{\tan\beta'}{1 - 2\varepsilon_{32}\sin\psi\tan\beta'} \tag{31}$$

In the same way as in the previous case, the total number of fillers must remain constant within the range $(\beta', \beta' + \mathrm{d}\beta') \times (\psi, \psi + \mathrm{d}\psi)$, that is:

$$\mathrm{d}N_{\substack{\beta',\beta'+\mathrm{d}\beta' \\ \psi,\psi+\mathrm{d}\psi}} = \mathrm{d}N_{\substack{\beta,\beta+\mathrm{d}\beta \\ \psi,\psi+\mathrm{d}\psi}} \tag{32}$$

Substituting Eq. (31) into Eq. (32), the resulting ODF, $p(\psi, \beta')$, is determined after some manipulation as:

$$p(\psi,\beta') = \left(1 - 4\varepsilon_{32}\sin\psi\sin\beta'\cos\beta' + 4\varepsilon_{32}^2\sin\psi\sin\beta'\right)^{-3/2} \tag{33}$$

Fig. 8 shows the ODF under distortion strain $\varepsilon_{32} = 0.1$. It is observed that the ODF has a symmetry about ψ. In addition, it is observed that the ODF gives more weight to fillers with polar angles β close to 0 , whilst lesser values are found for those with polar angles close to π. According to Fig. 7, fillers tend to align in the $\beta = 0$, $\psi = \pi/2$ direction. It is also noticeable that the limit cases of $\beta = 0, \pi$, and $\psi = 0, \pi$ correspond to unit ODF values. This fact is readily observed in Fig. 7 as these fillers do not experience any change in their orientation.

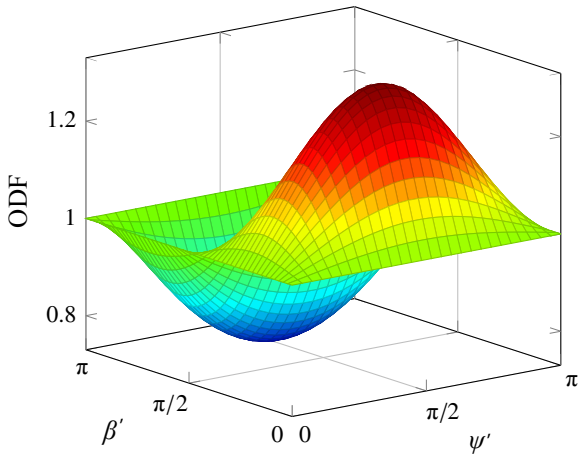

Figure 8: Variation of $p(\psi, \varphi)$ (ODF) with polar β and azimuthal angle ψ with distortion strain $\varepsilon_{32} = 0.1$ ($\nu = 0.45$).

3.2. Change in the conductive networks

On the basis of the previously obtained ODFs, the Komori-Makishima model in Eq. (20) can be readily applied to determine the influence of arbitrary strain cases on the percolation threshold. Uni-axial dilation and distortion conditions are shown in Fig. 9. Fig. 9 (a) shows the relative variation of the percolation threshold with respect to the unstrained value, f_c^o, for laterally constrained and unconstrained conditions. In both cases, compression/stretching leads to a loss of randomness of the nanofillers orientation distribution and, therefore, lesser probability of forming conductive paths. It is interesting to point out that, when the transverse displacements are constrained, the strain-induced variations of the percolation threshold are smaller that those computed with unconstrained conditions. Finally, it is worth noting that the variations are almost identical under compression ($\varepsilon < 0$) and tension ($\varepsilon > 0$), the latter yielding slightly lower values. On the other hand, Fig. 9 (b) shows the relative variation of the percolation threshold under distortion strain ε_{12}. In a similar way, the application of distortion yields losses in the randomness of the fillers orientation distribution and, consequently, increases in the percolation threshold. In this case, both positive and negative distortion strains lead to identical values.

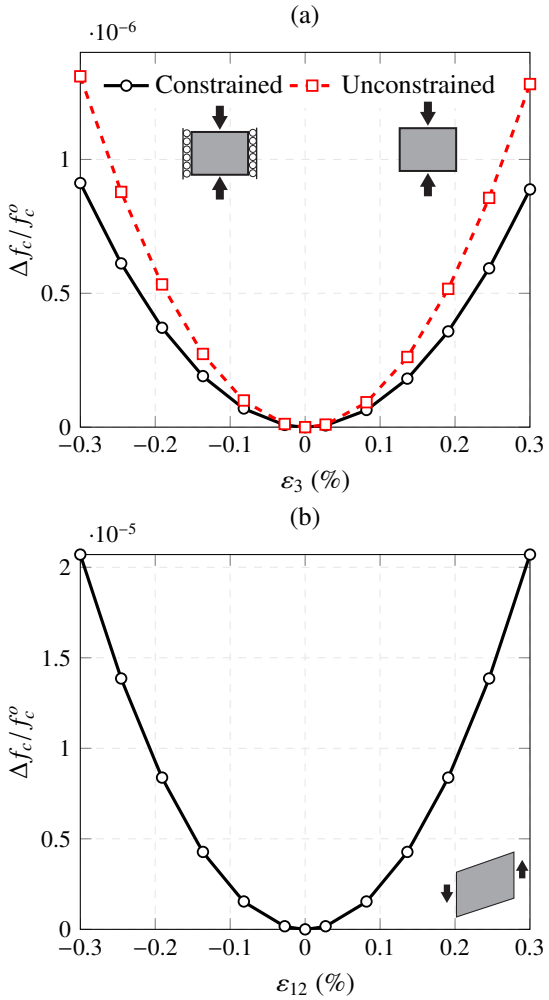

Figure 9: Variation of the percolation threshold with respect to the strain level ($\nu = 0.2$) under laterally constrained and unconstrained conditions (a) and distortion (b) assuming $L = 1$ μm , D=10 nm.

Fig. 10 depicts the variations of the ratio ξ/ξ_o with strain, being ξ_o and ξ the fraction of percolated CNTs (see Eq. (10)) before and after the application of strain, respectively. Conditions of laterally constrained and unconstrained uni-axial dilation with different Poisson's ratio are compared along with distortion conditions. Under tensile strains, it is observed that the amount of percolated nanotubes decreases with increasing strain. In this case, the loss of randomness of the fillers and the subsequent higher percolation thresholds, as well as the volume expansion, yield the breakage of electrically conductive paths. However, under compressive strains, these two mechanisms generate opposite effects [22]. Although the percolation threshold increases with higher compressive strains, the increase of the effective filler volume fraction dominates the small range of deformation and, therefore, increasing compressions imply larger numbers of conductive paths. In addition, laterally constrained and unconstrained conditions with different Poisson's ratios are compared. First, it is important to note that the constrained conditions exhibit greater variations in the number of percolated CNTs. As previously shown in Fig. 9, the percolation threshold increases more slowly, and also the strain-induced volume expansion has a greater effect in the case of laterally constrained systems. With regard to the effect of the Poisson's ratio for unconstrained systems, it is observed that decreasing Poisson's ratios lead to higher variations of the number of percolated CNTs. In particular, the limit case of $\nu = 0$ corresponds to the case of a laterally constrained system. In the case of shear strain, both positive and negative distortions generate the breakage of conductive paths. From a mathematical point of view, the variation of the percolation threshold solely contributes to the strain-sensitivity. The re-orientation of the fillers induced by shear strains always generates a loss of randomness of the filler orientation distribution and, thus, strains also cause increasing percolation thresholds and a decreasing number of conductive paths. Finally, Fig. 11 plots ξ/ξ_o versus uni-axial strain with laterally constrained and unconstrained conditions and different filler contents. It is noted that the fraction of percolated CNTs is more sensitive to strain for composites with lower CNT volume fraction.

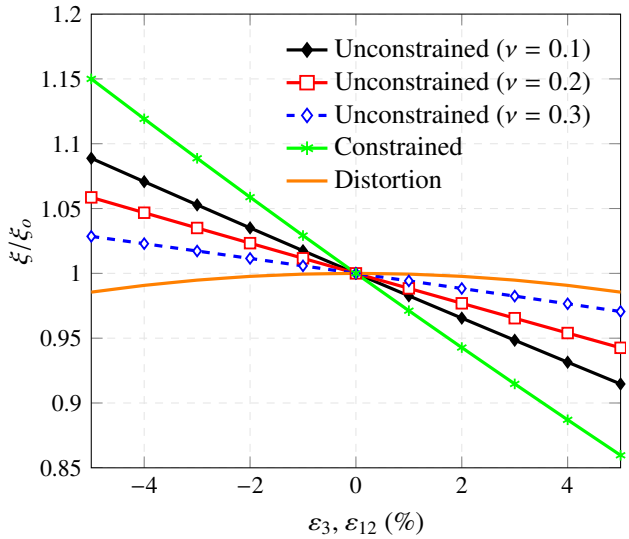

Figure 10: Variation of normalized percentage of percolated CNTs (ξ/ξ_o) versus strain for different strain conditions (f = 0.5%, L = 3 μm , D=15 nm).

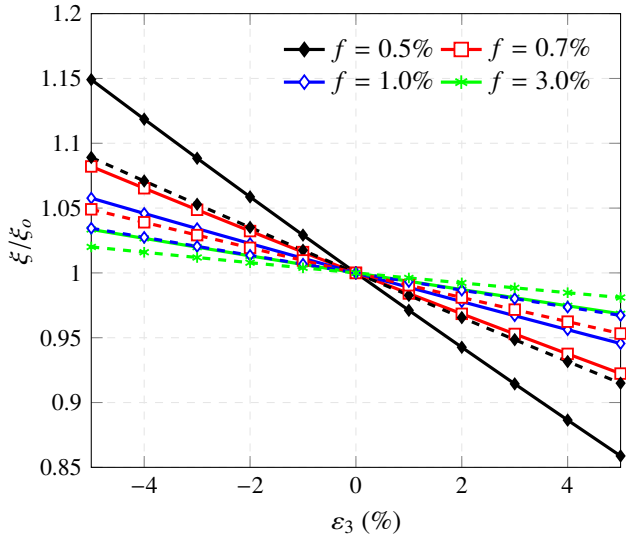

Figure 11: Variation of normalized percentage of percolated CNTs (ξ/ξ_o) versus strain for composites with different filler concentration and uni-axial dilation. (L = 3 μm , D=15 nm, ν = 0.2). Solid and dashed lines denote laterally constrained and unconstrained conditions.

3.3. Change in the tunneling resistance

There exists a gap in the literature on the determination of the inter-particle distance and the height of the potential barrier under general 3D strain states. In a simplified manner, the same hypothesis of linear dependence between the inter-particle distance and the height of the potential barrier with the strain in Eq. (21) is assumed for dilation cases. With regard to the distortion cases, the variation of the inter-particle properties is presumably smaller than under dilation and, due to the difficulty in its theoretical determination, it is simplified as strain independent. The importance of the strain-induced effects on the inter-particle properties, especially on the non-linear component of the response, was already discussed in previous work by the authors [22]. The determination of more accurate expressions for this quantity will need to be addressed in future work.

4. Steady-State Piezoresistivity analysis

Modeling the piezoresistive behavior of CNT-reinforced smart concretes under arbitrary 3D strain states requires linking the equations related to the electrical behavior of the material with those describing the mechanical

strain state, or alternatively the stress state assuming the material to behave as linear elastic. On the basis of the presented micromechanics approach, the electrical resistivity tensor $\boldsymbol{\rho}_{eff}$, which can be directly computed as the inverse of the conductivity tensor $\boldsymbol{\sigma}_{eff}$ in Eq. (11), i.e. $\boldsymbol{\rho}_{eff} = \boldsymbol{\sigma}_{eff}^{-1}$, relates the current intensity vector $\boldsymbol{J}$ to the electric field vector $\boldsymbol{E}$ as $\boldsymbol{E} = \boldsymbol{\rho}_{eff}\boldsymbol{J}$. This relation can be written in matrix notation as:

$$\begin{Bmatrix} E_1 \\ E_2 \\ E_3 \end{Bmatrix} = \begin{bmatrix} \rho_1 & \rho_6 & \rho_5 \\ \rho_6 & \rho_2 & \rho_4 \\ \rho_5 & \rho_4 & \rho_3 \end{bmatrix} \begin{Bmatrix} J_1 \\ J_2 \\ J_3 \end{Bmatrix} \tag{34}$$

When the composite is not subjected to any strain, the assumption of randomly oriented fillers leads to diagonal resistivity matrices with equal components ρ_0, i.e. $\rho_1 = \rho_2 = \rho_3 = \rho_0$ and $\rho_4 = \rho_5 = \rho_6 = 0$. After the application of strain, each component of the resistivity matrix changes. In general, the new components of the resistivity tensor can be written as follows:

$$\begin{Bmatrix} \rho_1 \\ \rho_2 \\ \rho_3 \\ \rho_4 \\ \rho_5 \\ \rho_6 \end{Bmatrix} = \begin{Bmatrix} \rho_0 \\ \rho_0 \\ \rho_0 \\ 0 \\ 0 \\ 0 \end{Bmatrix} + \begin{Bmatrix} \Delta\rho_1 \\ \Delta\rho_2 \\ \Delta\rho_3 \\ \Delta\rho_4 \\ \Delta\rho_5 \\ \Delta\rho_6 \end{Bmatrix} \tag{35}$$

which can be related to the strain in the composite through:

$$\boldsymbol{\rho}_{eff} = \boldsymbol{\rho}_{eff}^{o}\,(\boldsymbol{I} + \boldsymbol{r}) \tag{36}$$

where $\boldsymbol{\rho}_{eff}^{o} = (\boldsymbol{\sigma}_{eff}^{o})^{-1}$ is the resistivity matrix of the unloaded composite and $\boldsymbol{r}$ is the relative change in resistivity defined as $\boldsymbol{r} = \boldsymbol{\Pi}\boldsymbol{\varepsilon}$. The connection between the relative change in resistivity and the strain tensor is the $\boldsymbol{\Pi}$ matrix whose components are denoted as λ_{ij}. It is hypothesized that CNT-reinforced composites possess cubic crystal symmetry, similarly to silicon [55], and only three $\lambda-$coefficients are needed. Hence, $\boldsymbol{r} = \boldsymbol{\Pi}\boldsymbol{\varepsilon}$ in matrix notation becomes:

$$\begin{Bmatrix} \Delta\rho_1/\rho_0 \\ \Delta\rho_2/\rho_0 \\ \Delta\rho_3/\rho_0 \\ \Delta\rho_4/\rho_0 \\ \Delta\rho_5/\rho_0 \\ \Delta\rho_6/\rho_0 \end{Bmatrix} = \begin{bmatrix} \lambda_{11} & \lambda_{12} & \lambda_{12} & 0 & 0 & 0 \\ \lambda_{12} & \lambda_{11} & \lambda_{12} & 0 & 0 & 0 \\ \lambda_{12} & \lambda_{12} & \lambda_{11} & 0 & 0 & 0 \\ 0 & 0 & 0 & \lambda_{44} & 0 & 0 \\ 0 & 0 & 0 & 0 & \lambda_{44} & 0 \\ 0 & 0 & 0 & 0 & 0 & \lambda_{44} \end{bmatrix} \begin{Bmatrix} \varepsilon_1 \\ \varepsilon_2 \\ \varepsilon_3 \\ 2\varepsilon_{23} \\ 2\varepsilon_{13} \\ 2\varepsilon_{12} \end{Bmatrix} \tag{37}$$

Discussion on the correctness of this assumption is provided in subsequent parametric analyses. Among the three independent $\lambda-$coefficients in Eq. (37), λ_{11} depicts the piezoresistive effect along one principal crystal axis for strains applied in this principal crystal axis (longitudinal piezoresistive effect), λ_{12} relates the piezoresistive effect along one principal crystal axis for strains applied in one perpendicular crystal axis (transverse piezoresistive effect), and λ_{44} describes the piezoresistive effect on an out-of-plane electric field by the change of the in-plane current induced by in-plane shear stress. In order to compute the independent coefficients in $\boldsymbol{\Pi}$, only two virtual experiments are needed, namely laterally constrained uni-axial dilation and distortion as follows:

$$\begin{Bmatrix} \Delta\rho_1/\rho_0 \\ \Delta\rho_2/\rho_0 \\ \Delta\rho_3/\rho_0 \end{Bmatrix} = \begin{bmatrix} \lambda_{11} & \lambda_{12} & \lambda_{12} \\ \lambda_{12} & \lambda_{11} & \lambda_{12} \\ \lambda_{12} & \lambda_{12} & \lambda_{11} \end{bmatrix} \begin{Bmatrix} 0 \\ 0 \\ \varepsilon_3 \end{Bmatrix} = \boldsymbol{\Pi}^{dil} \begin{Bmatrix} 0 \\ 0 \\ \varepsilon_3 \end{Bmatrix} \tag{38}$$

$$\begin{Bmatrix} \Delta\rho_4/\rho_0 \\ \Delta\rho_5/\rho_0 \\ \Delta\rho_6/\rho_0 \end{Bmatrix} = \begin{bmatrix} \lambda_{44} & 0 & 0 \\ 0 & \lambda_{44} & 0 \\ 0 & 0 & \lambda_{44} \end{bmatrix} \begin{Bmatrix} 0 \\ 0 \\ 2\varepsilon_{12} \end{Bmatrix} = \boldsymbol{\Pi}^{dis} \begin{Bmatrix} 0 \\ 0 \\ 2\varepsilon_{12} \end{Bmatrix} \tag{39}$$

5. Numerical results and discussion

In this section, extensive parametric analyses are presented in order to improve understanding of the piezoresistive behavior of CNT-reinforced smart concretes in view of their applications for strain monitoring in RC structures. Further, discussion on the characterization of the piezoresistivity matrix is presented. Afterwards, a cubic CNT-reinforced mortar sensor is studied and compared with experimental data. In this way, a mathematically tractable model for cubic smart concrete strain sensors is achieved.

5.1. Parametric analyses

In this first set of analyses, detailed parametric studies have been carried out in order to give some insight into the structure of the proposed model, as well as to extract valuable conclusions for the design of self-sensing CNT-reinforced cement-based composites. For illustrative purposes, cement paste (PA) is chosen as matrix material with electrical conductivity 2.8×10^{-3} S/m. The reinforcing phase consists of Multi-Walled CNTs (MWCNTs) with electrical conductivities ranging from 10^0 to 10^7 S/m. The rest of the variables have been taken from reference [22] unless otherwise indicated.

5.1.1. Effects of constituents properties on the strain-induced electrical response

First, uni-axial laterally constrained dilation (ε_1,0,0) and distortion (ε_{12}) tests are conducted. Fig. 12 shows the relative change in resistivity $\Delta\rho/\rho_0$ of MWCNT-reinforced cement paste with different filler concentrations f. For illustrative purposes, the variation parameters of the inter-particle properties under dilation, C_1 and C_2, have been taken from [54] as 8.9045 and 0.0243, respectively. According to the physical properties of cement paste, the Poisson's ratio has been set to 0.2. The externally applied strain has been imposed in the range $(-500, +500)$ $\mu\varepsilon$. In a similar way to previous work by the authors [22], it is noted in Fig. 12 (a) that the proposed approach reproduces some of the effects evidenced in the experiments under uni-axial strain. For compressive loadings, $\varepsilon < 0$, the composites exhibit higher values of conductivity, unlike for tensile strains. In both cases, the percolation threshold increases, although, for the considered ranges of deformation, the effect of the volume expansion and variation of the inter-particle properties becomes predominant. Also, it is noticeable that for MWCNT concentrations below and above the percolation threshold, the strain-sensitivity of the composite is considerably low. On the contrary, filler concentrations close to the percolation threshold lead to the highest sensitivity values. This fact justifies the evidence from the experiments about the existence of a maximum strain-sensitivity around the percolation threshold as shown in reference [22] for laterally unconstrained conditions. Solid and dashed lines denote longitudinal ($\Delta\rho_1/\rho_0$) and transverse ($\Delta\rho_2/\rho_0 = \Delta\rho_3/\rho_0$) relative changes in resistivity, respectively. It is observed that transverse relative changes are very similar to the longitudinal ones. This fact indicates that the sensor provides almost the same output (in this case almost proportional to uni-axial strain) regardless of the layout of the electrodes. A closer inspection of the results reveals that the transverse sensitivity is slightly higher than the longitudinal one, a behavior that has been also observed in some previously published experimental works on similar strain-sensing materials (see e.g. Fig. 10 in reference [56]). This behavior finds an explanation in the re-orientation effect. For instance, in the case of tensile strains, fillers tend to align in the direction of the strain and, thus, the longitudinal resistivity experiences comparatively smaller reductions. This behavior can be also seen in Fig. 13, where the overall electric conductivity for different MWCNT concentrations and strain levels is represented. It is important to note that both longitudinal and transverse effective conductivities are close at the percolation threshold and differences raise as the filler concentration increases. This effect remarks the increasing role of filler-reorientation effect at higher filler contents. Fig. 12 (b) depicts the relative change in resistivity $\Delta\rho_6/\rho_0$ under shear strain ε_{12}. First, it is important to note that the strain sensitivity is considerably lower than in the dilation case. Moreover, the relative change in resistivity exhibits considerably linear variations with shear strain, desirable feature both for modeling and designing of strain-sensing composites. In this case, the strain sensitivity is higher with increasing filler contents. This fact can be readily ascribed to the isolated contribution of re-orientation effects, since the volume of the composite stays constant.

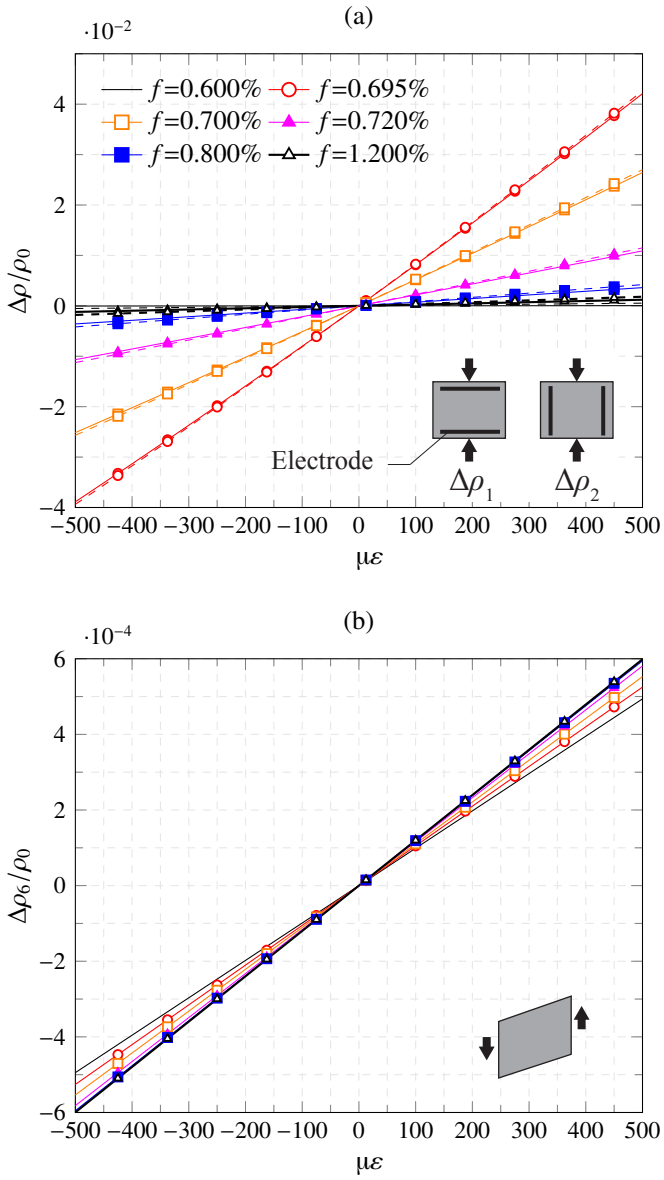

Figure 12: Strain-sensing capabilities of MWCNT-reinforced cement paste with different filler concentrations under laterally constrained uni-axial dilation (a) and distortion (b) (ν=0.2, L = 1 µm , D=10 nm, λ=0.36 eV, d_c=0.5 nm, σ_c = 10^4 S/m, C_1=8.9045, C_2=0.0243). Solid and dashed lines in (a) denote longitudinal, ($\Delta\rho_1/\rho_0$), and transverse, ($\Delta\rho_2/\rho_0$ = $\Delta\rho_3/\rho_0$), relative changes in resistivity, respectively.

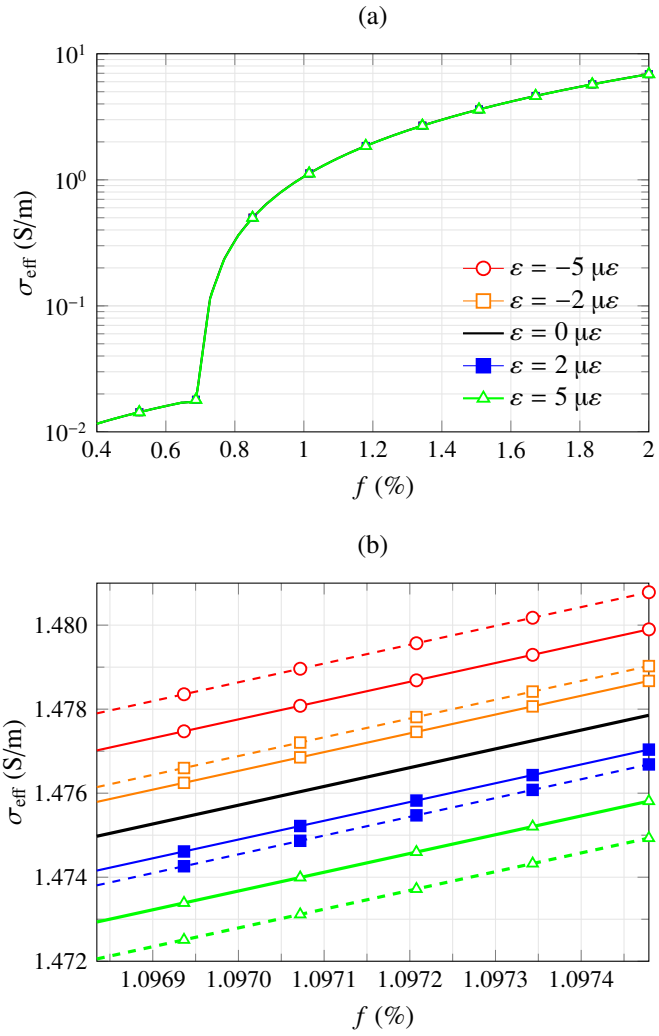

Figure 13: Overall electrical conductivity (a) and detail view (b) of MWCNT-reinforced cement paste under different laterally constrained uni-axial dilation levels (ν=0.2, L = 1 µm , D=10 nm, λ=0.36 eV, d_c=0.5 nm, σ_c = 10^7 S/m, C_1=8.9045, C_2=0.0243). Solid and dashed lines denote in-plane, $\sigma_{eff}(1,1)$, and normal, $\sigma_{eff}(1,2)$, electrical conductivities, respectively.

Fig. 14 is aimed at inspecting the differences between previous work by the authors [22] and the present approach, that is the comparison between uni-axial unconstrained ($\overline{\varepsilon}_1 = \overline{\varepsilon}_2 = \overline{\varepsilon}_3^{-\nu}$) and constrained dilations ($\overline{\varepsilon}_1 = \overline{\varepsilon}_2 = 1$). It is first noted that constrained conditions yield considerably higher electrical strain sensitivities. In spite of the fact that filler re-orientation is less influential in the case of constrained conditions as previously shown in Fig. 4, volume expansion effect is indeed more predominant as evidenced in Fig. 10, what explains the higher sensitivity for laterally constrained conditions. Furthermore, it is also observed here that the transverse sensitivities are slightly higher than the longitudinal ones in both conditions.

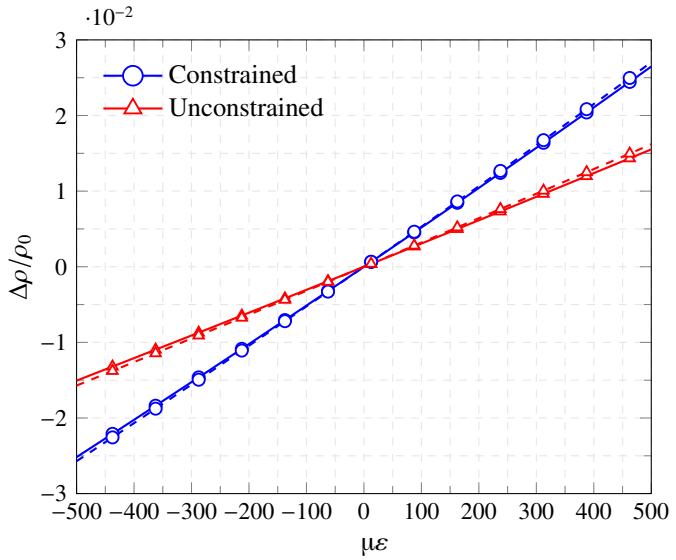

Figure 14: Strain-sensing capabilities of MWCNT-reinforced cement paste under uni-axial laterally constrained and unconstrained dilations (ν=0.2, L = 1 μm , D=10 nm, λ=0.36 eV, f = 0.7%, d_c=0.5 nm, σ_c = 10^4 S/m, C_1=8.9045, C_2=0.0243). Solid and dashed lines denote longitudinal, ($\Delta\rho_1/\rho_0$), and transverse, ($\Delta\rho_2/\rho_0$ = $\Delta\rho_3/\rho_0$), relative changes in resistivity, respectively.

Fig. 15 shows the relative resistance change for different values of MWCNT conductivity under laterally constrained uni-axial dilation. Four filler concentrations, namely f=0.6935%, f=0.7000%, f=1.0000% and f=2.0000%, are selected. Note that the filler content in Fig. 15 (a) is very close to the percolation threshold, and Figs. 15 (b) to (d) consider filler contents that are progressively further away from the percolation threshold of the unstrained system. It can be extracted from these figures that more conductive fillers lead to higher strain sensitivities. It is also important to note that nonlinearities, related to the coupled effect of the volume expansion and variation of the percolation threshold, gain importance for concentrations close to the unloaded percolation threshold. On the contrary, the strain-sensing curves exhibit more linear behaviors for concentrations far from this critical concentration. In other words, when the filler concentration is near the percolation threshold, the number of formed conductive paths is still limited so that the breakage or formation of conductive networks has a strong impact on the overall conductivity. However, when there exist many conductive paths, the variation of the number of paths does not lead to substantial differences and the composite is thus less piezoresistive. From a mathematical point of view, the strain-induced variations of the effective volume fraction and of the percolation threshold result in a variation of the fraction of percolated CNTs, ξ. Hence, the appearance of important nonlinear responses for concentrations close to the percolation threshold is justified by the piecewise definition of the percolation theory (see Eq. (11)). When percolation begins, i.e. for small values of ξ, the conductivity of CNT-reinforced nanocomposites experiences sharp increases. In this first region is where the strain-induced changes lead to the largest impacts and the composites exhibit the most nonlinear response, as it is the case for Fig. 15 (a). Once a sufficient number of conductive paths has been formed, the overall conductivity stabilizes and the composites respond to strain in a more linear way.

Fig. 16 shows the relative resistance change for different values of MWCNT conductivity under shear strain ε_{12}. In order to assess the correctness of the assumption of cubic crystal symmetry of the piezoresistivity matrix in Eq. (37), terms $\Delta\rho_6/\rho_o$ and $\Delta\rho_1/\rho_o$ are represented with solid and dashed lines, respectively. Four filler concentrations, namely f=0.6935%, f=0.7000%, f=1.0000% and f=2.0000%, are again selected here as filler contents. On the basis of the hypothesis of cubic crystal symmetry of the piezoresistivity matrix, when the composite is subjected to a shear strain ε_{12}, only variations in $\Delta\rho_6/\rho_o$ should be observed, whilst the rest of the terms should be constantly zero. However, it can be seen in Fig. 16 (a), defined with a filler content very close to the percolation threshold, that the term $\Delta\rho_1/\rho_o$ not only does not disappear but exhibits higher variations than $\Delta\rho_6/\rho_o$. Terms $\Delta\rho_2/\rho_o$ and $\Delta\rho_3/\rho_o$ are not included in this analysis for the sake of clarity as identical conclusions are extracted for them. This effect is ascribed to the re-orientation of the fillers which does not only affect the shear direction but also the rest of orientations. It is also noticeable that the term $\Delta\rho_6/\rho_o$ is highly linear with the shear strain, whilst diagonal terms of the resistivity matrix are highly non-linear. On the other hand, it can be seen in Figs. 16 (b) to (d) that variations of the diagonal terms of the resistivity matrix are drastically minimized for filler volume fractions above the percolation threshold. In these cases, the term $\Delta\rho_6/\rho_o$ is clearly shown dominant and linear with the strain. Overall, it can be concluded that the hypothesis of cubic crystal symmetry of the piezoresistivity

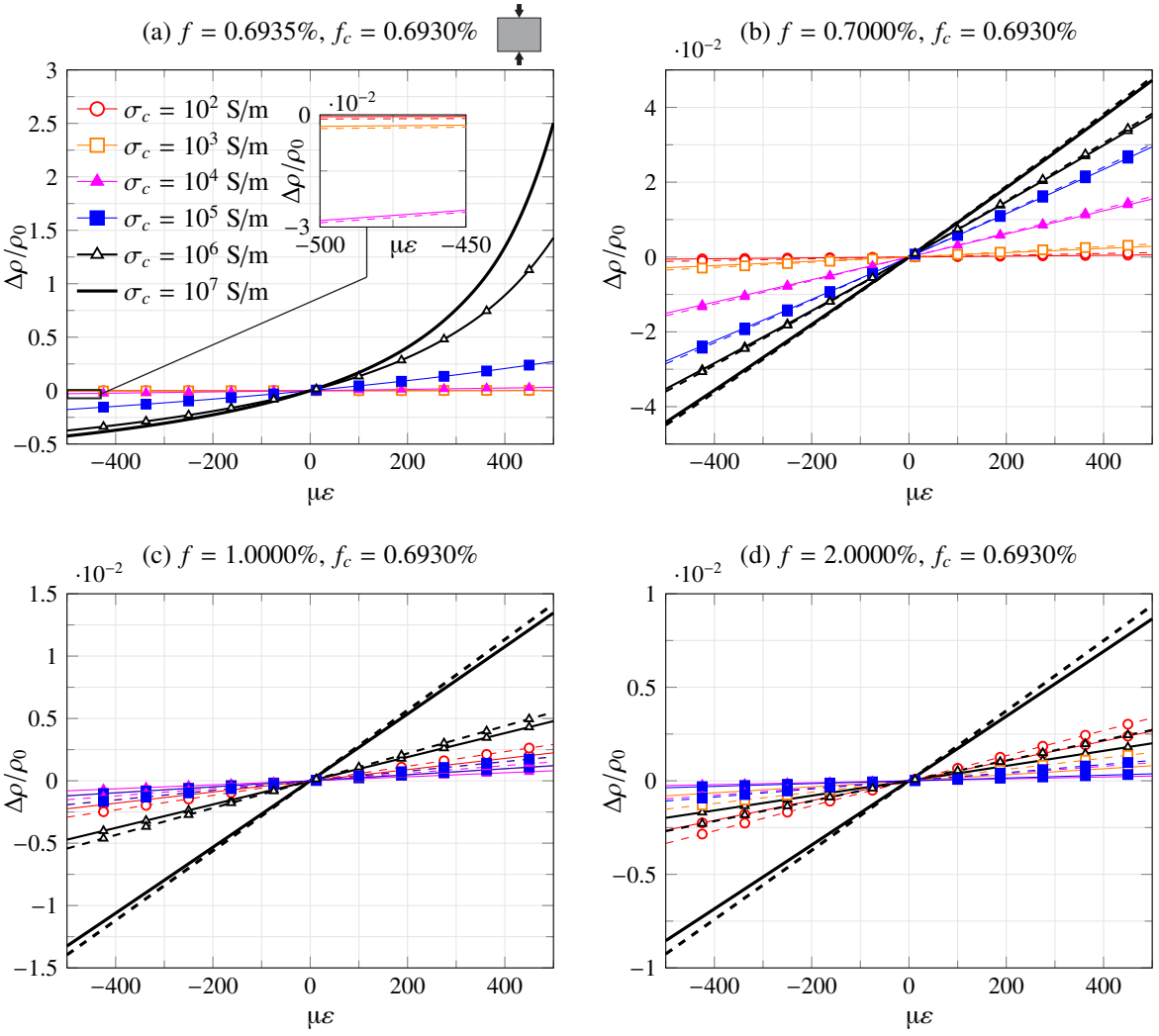

Figure 15: Strain-induced relative resistance change $\Delta\rho/\rho_o$ of MWCNT-reinforced cement paste for different filler conductivities σ_c and volume fractions, namely f=0.6935% (a), f=0.7000% (b), f=1.0000% (c), and f=2.0000% (d), under laterally constrained uniaxial dilation (ν=0.2, L = 1 μm , D=10 nm, λ=0.36 eV, d_c=0.5 nm, C_1=8.9045, C_2=0.0243). Solid and dashed lines denote longitudinal, ($\Delta\rho_1/\rho_0$), and transverse, ($\Delta\rho_2/\rho_0 = \Delta\rho_3/\rho_0$), relative changes in resistivity, respectively.

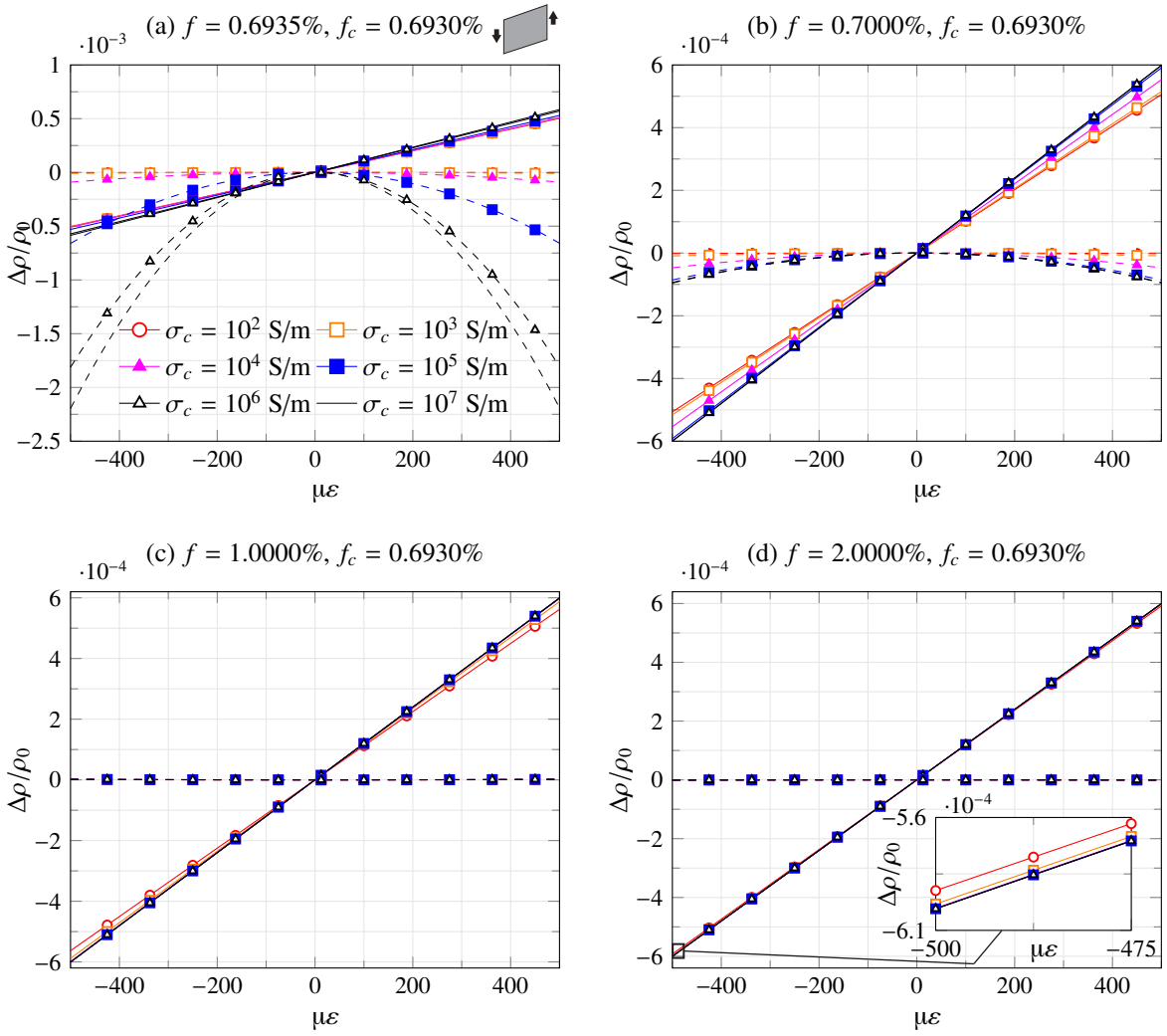

Figure 16: Strain-induced relative resistance change $\Delta\rho/\rho_o$ of MWCNT-reinforced cement paste for different filler conductivities σ_c and volume fractions, namely f=0.6935% (a), f=0.7000% (b), f=1.0000% (c), and f=2.0000% (d), under distortion strain ε_{12} (ν=0.2, L = 1 µm , D=10 nm, λ=0.36 eV, d_c=0.5 nm, C_1=0, C_2=0). Solid and dashed lines refer to $\Delta\rho_6/\rho_o$ and $\Delta\rho_1/\rho_o$ terms, respectively.

matrix fails to reproduce the response of CNT-reinforced cement-matrix composites at filler contents very close to the percolation threshold. Nonetheless, the variation of the diagonal terms of the resistivity matrix can be neglected for filler contents slightly higher than the percolation threshold. In these cases, the cubic crystal symmetry condition of the piezoresistivity matrix can be accepted, as well as the linearity of the piezoresistivity coefficient λ_{44}. Finally, let us remark that the sensitivity to shear strains increases with the filler content.

5.1.2. Characterization of the piezoresistivity matrix

In this section, the piezoresistivity coefficients are determined as the ratios between relative variations of electrical resistance and strain according to the virtual experiments in Eqs. (38) and (39). Fig. 17 depicts the piezoresistivity coefficients λ_{11} and λ_{12}, indicated by solid and dashed lines, as a function of the filler concentration. As previously shown, because of the peculiar electromechanical behavior of CNT-reinforced composites subjected to uni-axial dilation, λ_{11} is rate dependent and also varies with ε_1, resulting in a nonlinear relationship of strain-to-signal. According to some other previously published experimental and theoretical works [57], it has been shown in Fig. 15 that the strain-sensing curves can be approximately modeled with a first linear range followed by a nonlinear one. Although there are a few works dealing with the definition of the nonlinear part, such as the work of Park *et al.* [57] who defined it by an exponential-type function, the first linear stage is of high interest in the realm of SHM as the accuracy of the measurements is higher within this range. In this work, a linear regression based on a least squares estimator is adjusted in the strain range that leads to a coefficient of determination of 0.99. Hence, the piezoresistivity coefficients λ_{11} and λ_{12} are computed as the slope of the regression

of their corresponding strain-sensitivity curves. It is important to note that, according to the results in Fig. 12, maximum values of piezoresistivity coefficients λ_{11} are found in Fig. 17 around the percolation threshold. Also, as expected from Fig. 15, more conductive fillers lead to higher sensitivity coefficients. It is also noticeable that the maximum peaks are sharper for higher filler conductivities, whilst less conductive fillers lead to smoother curves. It is observed that λ_{12} exhibits slightly higher values along the whole range of filler concentrations as expected from previous analyses.

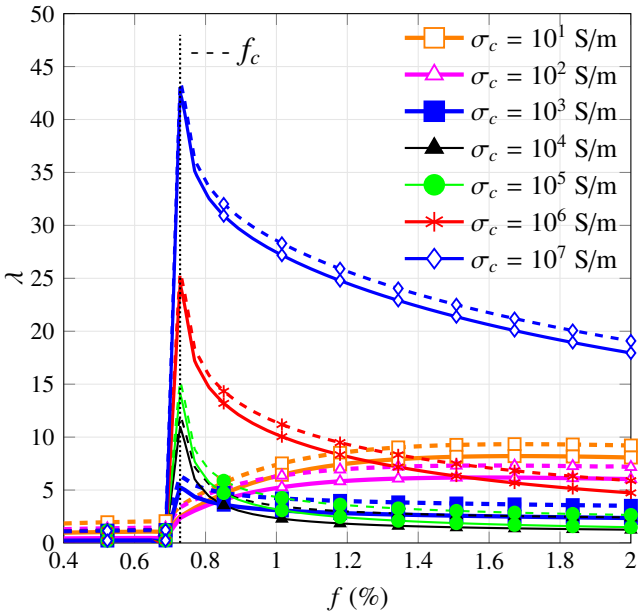

Figure 17: Piezoresistivity coefficients of MWCNT-reinforced cement paste versus filler concentration f under laterally constrained uni-axial compression for different filler conductivities σ_c (L = 1 µm , D=10 nm, λ=0.36 eV, d_c=0.56 nm, C_1=8.9045, C_2=0.0243). Solid and dashed lines stand for longitudinal and transverse strain gauges, λ_{11} and λ_{12}, respectively.

Fig. 18 shows the piezoresistivity coefficient λ_{44} for different filler conductivities. In this case, λ_{44} continuously increases with the filler content. A sharp increase in the sensitivity is found at filler contents around the percolation threshold after which slow increasing rates are detected. In a similar way to the previous analysis, more conductive fillers lead to higher sensitivity coefficients. Overall, it can be concluded that the piezoresistivity coefficients under shear strains, λ_{44}, are substantially lower than those associated to dilation. Finally, the piezoresistivity matrix can be computed according to Eq. (37). For instance, in the case of MWCNT-reinforced cement paste (PA) with filler volume fraction f = 1% and filler conductivity $\sigma_c = 10^6$ S/m, the piezoresistivity matrix $\mathbf{\Pi}$ reads:

$$\mathbf{\Pi} = \begin{bmatrix} \mathbf{\Pi}^{dil} & 0 \\ 0 & \mathbf{\Pi}^{dis} \end{bmatrix} = \left[\begin{array}{ccc:ccc} 10.04 & 11.19 & 11.19 & 0 & 0 & 0 \\ 11.19 & 10.04 & 11.19 & 0 & 0 & 0 \\ 11.19 & 11.19 & 10.04 & 0 & 0 & 0 \\ \hdashline 0 & 0 & 0 & 0.6 & 0 & 0 \\ 0 & 0 & 0 & 0 & 0.6 & 0 \\ 0 & 0 & 0 & 0 & 0 & 0.6 \end{array}\right] \tag{40}$$

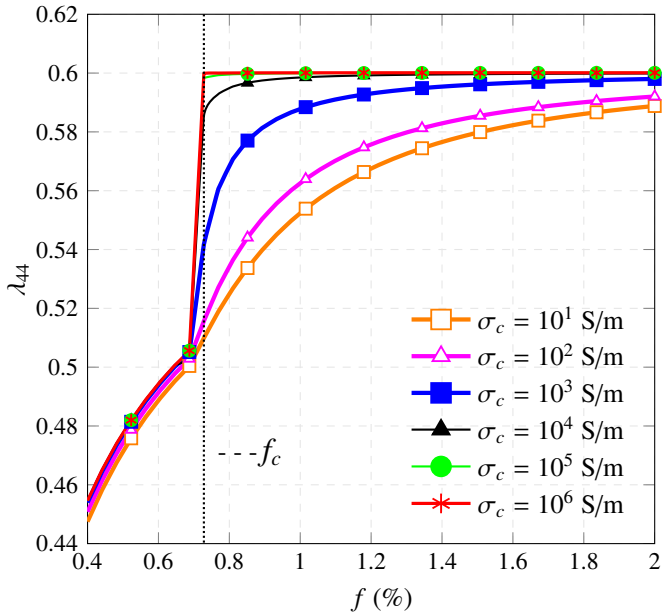

Figure 18: Piezoresistivity coefficient λ_{44} of MWCNT-reinforced cement paste versus filler concentration f under distortion strains ε_{12} for different filler conductivities σ_c (L = 1 µm , D=10 nm, λ=0.36 eV, d_c=0.56 nm).

In light of the similarity between λ_{11} and λ_{12}, as well as the small values of λ_{44}, it can be concluded that CNT-reinforced smart concretes are essentially sensitive to volumetric strain. It follows that cubes made of such multifunctional materials can be used as volumetric strain sensors to be embedded into concrete elements before casting. In particular, the relative change in electrical resistance outputted by similar sensors, whatever the deployment of electrodes, in a typical 2-probe or 4-probe configuration (see Fig. 19), can be approximated by means of a constant piezoresistivity coefficient or gauge factor λ as follows:

$$\frac{\Delta\rho}{\rho_o} = \frac{\Delta R}{R_o} \approx \lambda\,(\varepsilon_1 + \varepsilon_2 + \varepsilon_3) \tag{41}$$

with ΔR the variation of the electrical resistance of the specimen, and R_o the electrical resistance of the unloaded specimen.

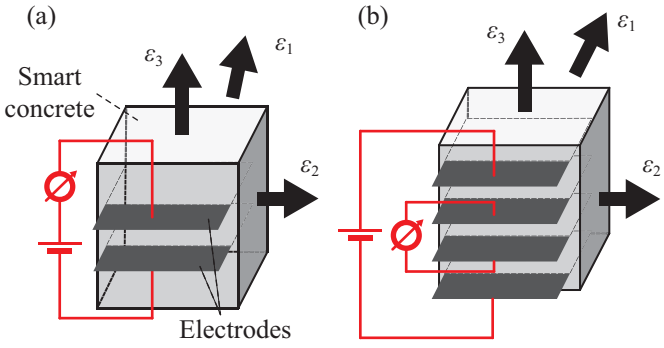

Figure 19: Schematic of 2-probe (a) and 4-probe (b) resistivity measurement setups.

5.2. FEM simulation of an embeddable smart block

In this section, a three-dimensional case study is presented in order to illustrate the combination of the proposed micromechanics approach with a FEM formulation. More specifically, a smart sensor made of self-sensing MWCNT-reinforced mortar subjected to laterally unconstrained quasi-static compressive loading has been modeled by the present micromechanics approach, introducing its mixed mechanical-electrical constitutive behavior within a FEM analysis. In the present work, the simulations have been carried out using the commercial software ANSYS v15.0 [58]. This case study was already analyzed in previous work by the authors [22]. On the basis of the experimental results in reference [59], the variables of the micromechanics model, including filler properties, waviness and agglomeration effects, were fitted by parametric studies with very good agreements. Let us

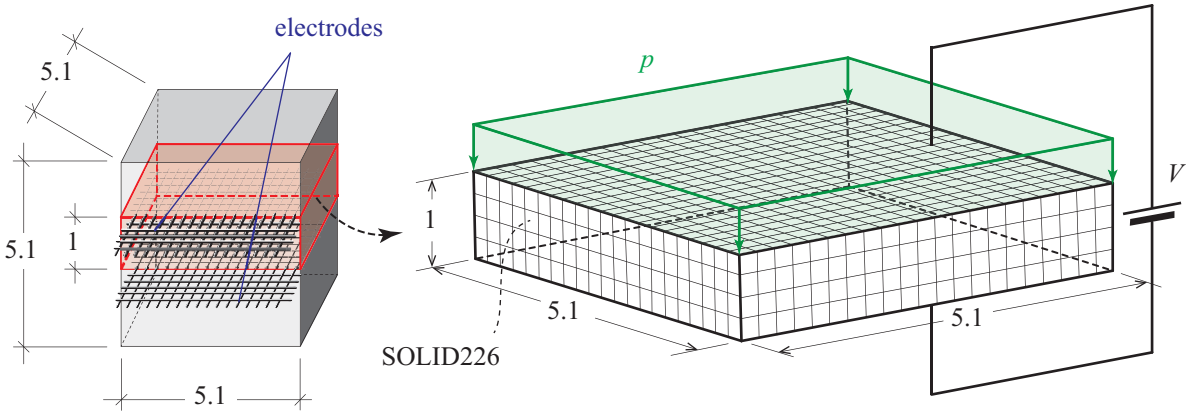

Figure 20: Geometry and dimensions of the self-sensing MWCNT-reinforced mortar and of the electrodes (units in cm) (a), and finite element modeling of the active region of the sensor (b).

recall that the scope of previous work was restricted to laterally unconstrained uni-axial compression/stretching. In this work, the piezoresistivity coefficients are determined for laterally constrained uni-axial compression and, afterwards, the electrical response is computed by a coupled electro-mechanical calculation in ANSYS. It is also important to note that, as previously demonstrated in [22], the strain sensitivity of CNT-reinforced cement-matrix composites is slightly different under compression and stretching. However, the difference between the piezoresistivity coefficients under compression and traction is small enough that a common strain sensitivity is assumed.

The sensor is a cube with sides of 5.1 cm instrumented with two stainless steel nets as electrodes, placed at a mutual distance of 1 cm as shown in Fig. 20 (a). The electrical conductivity of mortar is chosen as 1.04×10^{-3} S/m and MWCNTs are type Graphistrength C100 with electrical conductivities in the range 10^0 to 10^7 S/m. In particular, a sensor with filler content of 0.75% mass content with respect to mass of cement wt is selected. The mass content with respect to mass of cement can be related to the filler volume fraction as $wt = f\rho_N/m_{cem}$, with ρ_N and m_{cem} being the mass density of CNTs and the mass of cement per unit volume of the composite, equal to 50 kg/m^3 and 654 kg/m^3, respectively. Fig. 21 shows the electrical resistance as a function of the applied strain obtained in the experiments [59]. Furthermore, the theoretical results computed in previous work [22], denoted by "MA-1D", are plotted for a filler electrical conductivity of 10^4 S/m. In this work, the piezoresistivity coefficients have been computed under virtual experiments of laterally constrained uni-axial dilation and distortion as illustrated above. The rest of the micromechanical parameters of the model, including waviness and agglomeration effects, have been taken from reference [22] (readers are invited to refer to Figs. 26 and 27 in [22]). The active region of the sensor, defined as the material region between electrodes (5.1×5.1×1 cm), has been discretized for computational purposes as shown in Fig. 20 (b). Assuming that the electrodes are much more conductive than the composite, it is assumed that the electrodes can be modeled as a coupling condition of constant voltage on the upper and lower faces of the active region. Standard elements SOLID226, defined with twenty nodes and four degrees of freedom per node (three translations and an electric potential), have been chosen for the electromechanical numerical modeling. The experimental setup corresponds to a two-probe method, in which the lower electrode is grounded and the upper one is defined with a differential potential of 2.5 V. Finally, the Young's modulus and Poisson ratio of the composite are taken from the experiments as E=18 GPa and ν=0.2. By fitting the experimental results, inter-particle variation constants C_1=8.658, C_2=2.498 are computed and, accordingly, piezoresistivity coefficients λ_{11}=15.7, λ_{12}=16.20, λ_{44}=0.51 are obtained. It is observed in Fig. 21 that excellent agreements are found between the present approach and the experimental results, as well as with the previous theoretical model (MA-1D).

Once the consistency of the present micromechanics approach in conjunction with a FEM analysis has been demonstrated, a variety of applications where the strain state is three-dimensional in nature can be now handled. In order to illustrate this, Fig. 22 (a) shows a more sophisticated model of the previous sensor. In this case, the electrodes are modeled in detail accounting for their geometry, the penetration depth of the electrodes into the specimen, as well as the influence of the material region surrounding the active region. Fig. 22 (b) shows the electric potential field computed by the present mixed micromechanics-FEM approach. This type of results opens a vast range of applications such as the optimization of the electrodes configuration, different sensor geometries, presence of damages, and simulation of sensors' embedding into full-scale RC structural components.

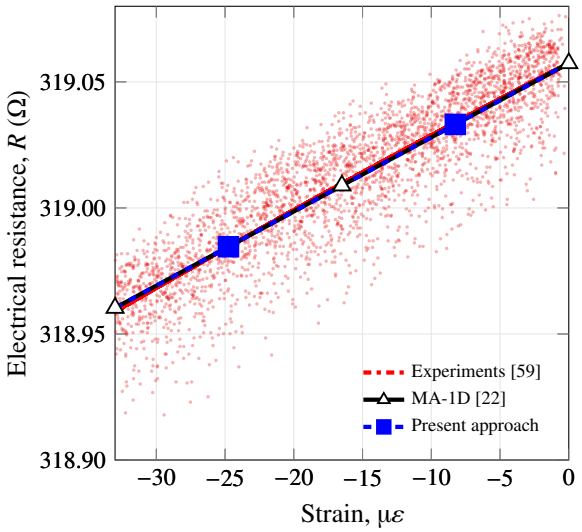

Figure 21: Comparison of the theoretical predictions and the experimental electrical resistance versus applied strain for mortar specimens with MWCNT concentration of 0.75% with respect to cement weight (λ_{11}=15.7, λ_{12}=16.20, λ_{44}=0.51, L = 0.25 μm , D=10 nm, λ=0.56 eV, d_c=1.8 nm, χ=0.68, ζ=0.90, θ=40°, C_1=8.658, C_2=2.498). MA-1D stands for the micromechanics approach of laterally unconstrained compression presented in reference [22].

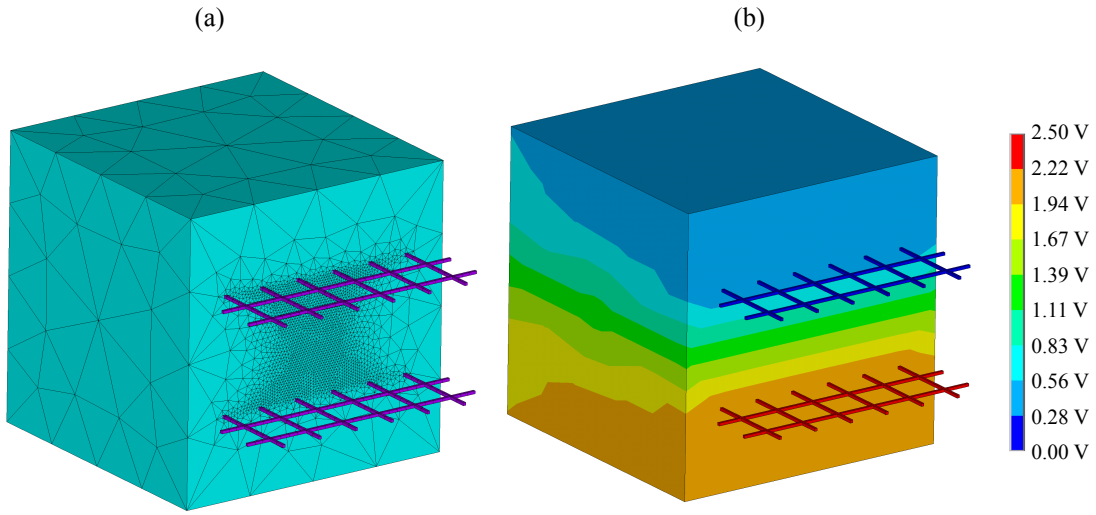

Figure 22: Detailed finite element model of MWCNT-reinforced mortar sensor (a), and electric potential field when a differential potential of 2.5 V is applied between the electrodes (b).

6. Conclusions

This paper has presented a micromechanics approach in combination with a finite element formulation for the analysis of the response of CNT-reinforced smart concrete sensors subjected to arbitrary 3D strain states. The two mechanisms that contribute to the conductivity of CNT composites, namely electron hopping and conductive networking, have been considered in a mixed micromechanics framework. The origin of the piezoresistive response of these composites is ascribed to (i) strain-induced changes in the volume fraction, (ii) changes in the conductive networks due to filler reorientation and, finally, (iii) changes in the tunneling resistance through variation of the inter-particle properties. New closed-form expressions of the ODFs for random arrangements of fillers under arbitrary dilation and distortion have been presented. On this basis, the variation of the percolation threshold is directly related to the ODFs by means of the Komori and Makishima model. Also, assuming that CNT-reinforced composites possess a cubic crystal symmetry, only three independent piezoresistivity coefficients are necessary to fully define the piezoresistivity matrix. The proposed approach has been shown capable of determining the piezoresistivity coefficients by two virtual tests, namely laterally constrained dilation and distortion. Afterwards, utilizing the computed piezoresistivity matrix within a multiphysics FE formulation, using a commercial computational environment, it has been shown possible to analyze three-dimensional CNT-reinforced structures. Detailed parametric analyses have been presented in order to illustrate the influence of the different properties of the constituents on the strain-sensing response of CNT-reinforced smart concretes. Finally, the accuracy of the proposed approach has been demonstrated by comparison with published experimental data.

The main contributions of this paper are summarized below:

- It has been shown that the dilation strain sensitivities of CNT-reinforced cement-based composites along the longitudinal (λ_{11}) and transverse (λ_{12}) directions are very similar, with slightly higher sensitivities in the transverse direction.
- The results showed that strains do not only generate variations of the shear components of the resistivity matrix but also of the diagonal terms. It has been shown that the interaction between shear strains and longitudinal/transverse resistivity terms is highly non-linear. However, for filler contents immediately above the percolation threshold, these terms disappear and the assumption of cubic crystal symmetry becomes valid. Overall, it has been shown that CNT-reinforced cement-based composites are also weakly sensitive to shear strains.
- Due to the similarities between the longitudinal and transverse piezoresistivity coefficients, as well as the low sensitivity under distortion, smart concrete strain sensors can be approximately modeled as volumetric strain sensors with one single piezoresistivity coefficient or gauge factor. This simplified model is ready to be applied in practical applications dealing with the use of smart concrete sensors embedded into RC structural components.
- The results of the parametric study have shown that the dilation piezoresistivity coefficients reach their maximum values for filler volume fractions at the percolation threshold. On the other hand, the shear piezoresistivity coefficients continuously increase with the filler content.
- Very close agreements of the present approach with experimental data from previous work have been reported. In addition, a comparison with previous theoretical results considering the ODFs of laterally unconstrained compression demonstrates the consistency of the assumptions imposed on the structure of the piezoresistivity matrix.

The presented micromechanics model is envisaged to provide a valuable tool for the analysis of three-dimensional CNT-reinforced cement-matrix composites, including simulation of the embedding of smart concrete sensors into full-scale RC components, smart sensing skins, self-sensing structural members, etc. The proposed theoretical framework is efficient in terms of computational cost and, more importantly, it models the complex coupled electro-mechanical behavior of smart concretes on a well founded physical basis. From here, further research can be pursued on more accurate definitions of the inter-particle properties and their variation with strain. Also, future work will require conducting more experimental tests on specimens under different loading conditions, including laterally constrained and un-constrained compression tests, different configurations of electrodes, bi-compression tests, as well as distortion tests, in order to provide a further validation of the proposed micromechanics approach.

Acknowledgement

This work was supported by the Ministerio de Economía y Competitividad of Spain and the Consejería de Economía, Innovación, Ciencia y Empleo of Andalucía (Spain) under projects DPI2014-53947-R and P12-TEP-2546. The support of the Italian Ministry of Education, University and Research (MIUR) through the

funded project of national interest "SMART-BRICK: novel strain-sensing nanocomposite clay brick enabling self-monitoring masonry structures" (Protocol No. 2015M55L27) is also gratefully acknowledged. E. G-M was also supported by a FPU contract-fellowship from the Spanish Ministry of Education Ref: FPU13/04892.

References

[1] A. D. B. Ferreira, P. R. Nóvoa, A. T. Marques, Multifunctional material systems: A state-of-the-art review, Composite Structures (2016).

[2] J. Wang, L. Zhang, K. Liew, Multiscale simulation of mechanical properties and microstructure of CNT-reinforced cement-based composites, Computer Methods in Applied Mechanics and Engineering 319 (2017) 393–413.

[3] J. Wang, L. Zhang, K. Liew, A multiscale modeling of CNT-reinforced cement composites, Computer Methods in Applied Mechanics and Engineering 309 (2016) 411–433.

[4] B. Han, B. Han, J. Ou, Experimental study on use of nickel powder-filled portland cement-based composite for fabrication of piezoresistive sensors with high sensitivity, Sensors and Actuators A: Physical 149 (2009) 51–55.

[5] F. Ubertini, A. L. Materazzi, A. D'Alessandro, S. Laflamme, Natural frequencies identification of a reinforced concrete beam using carbon nanotube cement-based sensors, Engineering Structures 60 (2014) 265–275.

[6] A. Downey, A. D'Alessandro, M. Baquera, E. García-Macías, D. Rolfes, F. Ubertini, S. Laflamme, R. Castro-Triguero, Damage detection, localization and quantification in conductive smart concrete structures using a resistor mesh model, Engineering Structures 148 (2017) 924–935.

[7] O. Galao, F. Baeza, E. Zornoza, P. Garcés, Strain and damage sensing properties on multifunctional cement composites with CNF admixture, Cement and concrete composites 46 (2014) 90–98.

[8] F. Ubertini, S. Laflamme, A. D'Alessandro, Smart cement paste with carbon nanotubes, Innovative Developments of Advanced Multifunctional Nanocomposites in Civil and Structural Engineering (2016) 97–120.

[9] B. Han, S. Ding, X. Yu, Intrinsic self-sensing concrete and structures: A review, Measurement 59 (2015) 110–128.

[10] S. P. Shah, M. Konsta-Gdoutos, Z. Metaxa, P. Mondal, Nanoscale modification of cementitious materials, in: Nanotechnology in Construction 3, Springer, 2009, pp. 125–130.

[11] B. Han, X. Yu, J. Ou, Multifunctional and smart carbon nanotube reinforced cement-based materials, in: Nanotechnology in civil infrastructure, Springer, 2011, pp. 1–47.

[12] B. Han, Y. Wang, S. Dong, L. Zhang, S. Ding, X. Yu, J. Ou, Smart concretes and structures: A review, Journal of intelligent material systems and structures 26 (2015) 1303–1345.

[13] B. Chen, K. Wu, W. Yao, Conductivity of carbon fiber reinforced cement-based composites, Cement and Concrete Composites 26 (2004) 291–297.

[14] M. Chiarello, R. Zinno, Electrical conductivity of self-monitoring CFRC, Cement and Concrete Composites 27 (2005) 463–469.

[15] S. Wen, D. Chung, Double percolation in the electrical conduction in carbon fiber reinforced cement-based materials, Carbon 45 (2007) 263–267.

[16] S. Wen, D. Chung, Carbon fiber-reinforced cement as a thermistor, Cement and Concrete Research 29 (1999) 961–965.

[17] H. Li, H. Xiao, J. Ou, Effect of compressive strain on electrical resistivity of carbon black-filled cement-based composites, Cement and Concrete Composites 28 (2006) 824–828.

[18] L. Chang, K. Friedrich, L. Ye, P. Toro, Evaluation and visualization of the percolating networks in multi-wall carbon nanotube/epoxy composites, Journal of materials science 44 (2009) 4003–4012.

[19] C. Feng, L. Jiang, Investigation of uniaxial stretching effects on the electrical conductivity of CNT-polymer nanocomposites, Journal of Physics D: Applied Physics 47 (2014) 405103.

[20] N. Hu, H. Fukunaga, S. Atobe, Y. Liu, J. Li, Piezoresistive strain sensors made from carbon nanotubes based polymer nanocomposites, Sensors 11 (2011) 10691–10723.

[21] T. Tallman, K. Wang, An arbitrary strains carbon nanotube composite piezoresistivity model for finite element integration, Applied Physics Letters 102 (2013) 011909.

[22] E. García-Macías, A. D'Alessandro, R. Castro-Triguero, D. Pérez-Mira, F. Ubertini, Micromechanics modeling of the uniaxial strain-sensing property of carbon nanotube cement-matrix composites for SHM applications, Composite Structures 163 (2017) 195–215.

[23] B. Zhang, Z. Zhou, K. Zhang, G. Yan, Z. Xu, Sensitive skin and the relative sensing system for real-time surface monitoring of crack in civil infrastructure, Journal of intelligent material systems and structures 17 (2006) 907–917.

[24] K. Loh, T. Hou, J. Lynch, N. Kotov, Nanotube-based sensing skins for crack detection and impact monitoring of structures, in: Proceedings of the 6th International Workshop on Structural Health Monitoring, Stanford, CA, USA, p. 16851692.

[25] N. Hu, Y. Karube, M. Arai, T. Watanabe, C. Yan, Y. Li, Y. Liu, H. Fukunaga, Investigation on sensitivity of a polymer/carbon nanotube composite strain sensor, Carbon 48 (2010) 680–687.

[26] R. Howser, H. Dhonde, Y. Mo, Self-sensing of carbon nanofiber concrete columns subjected to reversed cyclic loading, Smart materials and structures 20 (2011) 085031.

[27] M. S. Konsta-Gdoutos, C. A. Aza, Self sensing carbon nanotube (CNT) and nanofiber (CNF) cementitious composites for real time damage assessment in smart structures, Cement and Concrete Composites 53 (2014) 162–169.

[28] F. Deng, Q. S. Zheng, An analytical model of effective electrical conductivity of carbon nanotube composites, Applied Physics Letters 92 (2008) 071902.

[29] T. Takeda, Y. Shindo, Y. Kuronuma, F. Narita, Modeling and characterization of the electrical conductivity of carbon nanotube-based polymer composites, Polymer 52 (2011) 3852–3856.

[30] C. Feng, L. Jiang, Micromechanics modeling of the electrical conductivity of carbon nanotube (CNT)–polymer nanocomposites, Composites Part A: Applied Science and Manufacturing 47 (2013) 143–149.

[31] L. Y. Alamusi, N. Hu, Numerical simulations on piezoresistivity of CNT/polymer based nanocomposites, Computers Materials & Continua 20 (2010) 101–117.

[32] N. Hu, Y. Karube, C. Yan, Z. Masuda, H. Fukunaga, Tunneling effect in a polymer/carbon nanotube nanocomposite strain sensor, Acta Materialia 56 (2008) 2929–2936.

[33] J. G. Simmons, Electric tunnel effect between dissimilar electrodes separated by a thin insulating film, Journal of applied physics 34 (1963) 2581–2590.

[34] M. Taya, W. Kim, K. Ono, Piezoresistivity of a short fiber/elastomer matrix composite, Mechanics of materials 28 (1998) 53–59.

[35] A. Celzard, E. McRae, C. Deleuze, M. Dufort, G. Furdin, J. Marêché, Critical concentration in percolating systems containing a high-aspect-ratio filler, Physical Review B 53 (1996) 6209.

[36] C. Feng, L. Jiang, Micromechanics modeling of bi-axial stretching effects on the electrical conductivity of CNT-polymer composites, International Journal of Applied Mechanics 7 (2015) 1550005.

[37] J. Wang, W. Wang, C. Zhang, W. Yu, The electro-mechanical behavior of conductive filler reinforced polymer composite undergone large deformation: A combined numerical-analytical study, Composites Part B: Engineering (2017).

[38] E. García-Macías, A. D'Alessandro, R. Castro-Triguero, D. Pérez-Mira, F. Ubertini, Micromechanics modeling of the electrical conductivity of carbon nanotube cement-matrix composites, Composites Part B: Engineering 108 (2017) 451–469.

[39] S. Nemat-Nasser, M. Hori, Micromechanics: overall properties of heterogeneous materials, volume 37, Elsevier, 2013.

[40] S. Wen, D. Chung, Effect of carbon fiber grade on the electrical behavior of carbon fiber reinforced cement, Carbon 39 (2001) 369–373.

[41] J. G. Simmons, Generalized formula for the electric tunnel effect between similar electrodes separated by a thin insulating film, Journal of Applied Physics 34 (1963) 1793–1803.

[42] G. D. Seidel, D. C. Lagoudas, A micromechanics model for the electrical conductivity of nanotube-polymer nanocomposites, Journal of Composite Materials 43 (2009) 917–941.

[43] K. Yan, Q. Xue, Q. Zheng, L. Hao, The interface effect of the effective electrical conductivity of carbon nanotube composites, Nanotechnology 18 (2007) 255705.

[44] T. Mori, K. Tanaka, Average stress in matrix and average elastic energy of materials with misfitting inclusions, Acta metallurgica 21 (1973) 571–574.

[45] G. Odegard, T. Gates, Constitutive modeling of nanotube/polymer composites with various nanotube orientation, in: 2002 SEM Annual Conference on Experimental and Applied Mechanincs.

[46] M. Taya, Electronic composites: modeling, characterization, processing, and MEMS applications, Cambridge University Press, 2005.

[47] V. Kumar, A. Rawal, Tuning the electrical percolation threshold of polymer nanocomposites with rod-like nanofillers, Polymer 97 (2016) 295–299.

[48] T. Komori, K. Makishima, Numbers of fiber-to-fiber contacts in general fiber assemblies, Textile Research Journal 47 (1977) 13–17.

[49] W. Shim, Y. Kwon, S. Jeon, W. Yu, Optimally conductive networks in randomly dispersed CNT: graphene hybrids, Scientific reports 5 (2015).

[50] H. Corte, O. Kallmes, Statistical geometry of a fibrous network, in: The Formation and Structure of Paper, 1962, pp. 13–46.

[51] S. Toll, Packing mechanics of fiber reinforcements, Polymer Engineering & Science 38 (1998) 1337–1350.

[52] X. Zheng, M. G. Forest, R. Vaia, M. Arlen, R. Zhou, A strategy for dimensional percolation in sheared nanorod dispersions, Advanced Materials 19 (2007) 4038–4043.

[53] Y. Kuronuma, T. Takeda, Y. Shindo, F. Narita, Z. Wei, Electrical resistance-based strain sensing in carbon nanotube/polymer composites under tension: analytical modeling and experiments, Composites Science and Technology 72 (2012) 1678–1682.

[54] A. Sobha, S. K. Narayanankutty, Improved strain sensing property of functionalised multiwalled carbon nanotube/polyaniline composites in TPU matrix, Sensors and Actuators A: Physical 233 (2015) 98–107.

[55] G. K. Johns, Modeling piezoresistivity in silicon and polysilicon, Journal of Applied Engineering Mathematics April 2 (2006) 1–5.

[56] A. Downey, A. D'Alessandro, S. Laflamme, F. Ubertini, Smart bricks for strain sensing and crack detection in masonry structures, Smart Materials and Structures 27 (2017) 015009.

[57] M. Park, H. Kim, J. P. Youngblood, Strain-dependent electrical resistance of multi-walled carbon nanotube/polymer composite films, Nanotechnology 19 (2008) 055705.

[58] Structural analysis guide, Release 15.0, ANSYS Inc, Cannonsburg, PA (2014).

[59] A. D'Alessandro, M. Rallini, F. Ubertini, A. L. Materazzi, J. M. Kenny, Investigations on scalable fabrication procedures for self-sensing carbon nanotube cement-matrix composites for SHM applications, Cement and Concrete Composites 65 (2016) 200–213.